EBL FABRICATED PLASMONIC NANOSTRUCTURES FOR SENSING APPLICATIONS

A THESIS

SUBMITTED TO THE DEPARTMENT OF ELECTRICAL AND ELECTRONICS ENGINEERING

AND THE GRADUATE SCHOOL OF ENGINEERING AND SCIENCE

OF BILKENT UNIVERSITY

IN PARTIAL FULFILLMENT OF THE REQUIREMENTS

FOR THE DEGREE OF

DOCTOR OF PHILOSOPHY

By

Neval A. CİNEL

January, 2013

I certify that I have read this thesis and that in my opinion it is fully adequate, in scope and in quality, as a thesis for the degree of Doctor of Philosophy.

Prof. Dr. Ekmel Özbay (Supervisor)

I certify that I have read this thesis and that in my opinion it is fully adequate, in scope and in quality, as a thesis for the degree of Doctor of Philosophy.

Prof. Dr. Orhan Aytür

I certify that I have read this thesis and that in my opinion it is fully adequate, in scope and in quality, as a thesis for the degree of Doctor of Philosophy.

Assoc. Prof. Dr. Gülay Ertaş

I certify that I have read this thesis and that in my opinion it is fully adequate, in scope and in quality, as a thesis for the degree of Doctor of Philosophy.

Assist. Prof. Dr. F. Ömer İlday

I certify that I have read this thesis and that in my opinion it is fully adequate, in scope and in quality, as a thesis for the degree of Doctor of Philosophy.

Assist. Prof. Dr. Ali Kemal Okyay

Approved for the Graduate School of Engineering and Science:

Prof. Dr. Levent Onural

Director of the Graduate School of Engineering and Science

ABSTRACT

EBL FABRICATED PLASMONIC NANOSTRUCTURES FOR SENSING APPLICATIONS

Neval A. Cinel

Ph.D. in Electrical and Electronics Engineering

Supervisor: Prof. Dr. Ekmel Özbay

January, 2013

Plasmonics is a major branch of photonics dealing with light-matter interactions in metallic nanostructures. Plasmonic devices provide extreme confinement of electromagnetic oscillations to very small volumes beyond diffraction limit at optical frequencies. Our aim in this thesis study is to demonstrate the utilization of plasmonics for several applications such as optical localized surface plasmon resonance (LSPR) biosensor design, enhancement of signal intensity in surface enhanced Raman spectroscopy (SERS) and absorption enhancement in photodetectors.

Firstly, a sensor structure that detects the changes in the refractive index of the surrounding medium by optical transmission measurements was designed. Periodic silver nano-disk arrays on sapphire substrate written by Electron-Beam Lithography (EBL) were used for this aim. Optical characterization was done through transmission/reflection measurements and supported by finite difference time domain (FDTD) simulations. The sensor was first verified by a biotin-avidin bioassay. Real time binding studies showed that the sensor response was saturated within the first 30 minutes of application. Concentration dependency of the sensor structure showed an adequate response at the 1 nM-100 nM range.

The refractive index sensitivity of the sensor was determined as 354 nm/RIU. The idea was finally applied to the detection of heat killed E.Coli bacteria. Promising results that indicate the possibility of using the sensor for bacteria detection was obtained. Secondly, tandem truncated nano-cones composed of Au-SiO_2-Au layers that exhibit highly tunable double resonance behavior were shown to increase SERS signal intensity, for the first time. Enhancement factor (EF) calculations indicated an enhancement factor of 3.86 $x10^7$. The double resonance design showed a 10 fold better enhancement when compared to its single resonance counterpart. This enhancement is believed to be even more prominent for applications such as NIR-SERS and Surface Enhanced Hyper Raman Scattering (SEHRS). Another SERS substrate containing dual layer, periodic, "coupled" concentric rings, separated by a dielectric spacer provided Raman signal intensity 630 times larger than plain gold film and 8 times larger than an "etched" concentric ring structure. The design provided an enhancement factor of $1.67x10^7$. Finally, Al nanoparticles with plasmonic resonance at UV wavelengths fabricated in between the Schottky contacts of an MSM detector on semi-insulating GaN was shown to yield 1.5 fold enhancement in absorption and photocurrent collection. Plasmonic enhancement in UV was studied for the first time with this study. Another UV-MSM photodetector on GaN that includes subwavelength apertures surrounded by nano-structured metal gratings was compared to a conventional design without gratings. Results indicated an 8 fold enhancement in the photocurrent at the resonant wavelength.

Keywords: plasmonics, surface plasmon polariton, nano-particle, localized surface plasmon resonance, Surface Enhanced Raman Spectroscopy (SERS)

ÖZET

EIL İLE ALGILAMA UYGULAMALARI İÇİN PLAZMONİK NANOYAPILARIN GELİŞTİRİLMESİ

Neval A. Cinel

Elektrik-Elektronik Mühendisliği, Doktora

Tez Yöneticisi: Prof. Dr. Ekmel Özbay

January, 2013

Plazmonik, fotoniğin metalik nanoyapılardaki ışık-madde etkileşimlerini ele alan önemli bir dalıdır. Plazmonik aygıtlar, optik frekanslarda, kırınım sınırının ötesinde, elektromanyetik salınımların çok küçük hacimlere hapsine imkan verir. Bu tez çalışmasında amacımız, optik localize yüzey plasmon resonans (LYPR) biyosensörü tasarımı, yüzeyde zenginleştirilmiş Raman spektroskopisinde (YZRS) Raman sinyalinin iyileştirilmesi ve fotodedektörlerde soğurumun iyileştirilmesinde plazmonikten yararlanılabileceğini göstermektir.

İlk olarak, çevresel ortamdaki kırılma indisi değişikliklerini optik geçirim ölçümleri ile tespit eden bir sensör yapısı tasarlandı. Elektron Işın Demeti litografisi ile safir alttaş üzerine yazılan periyodik gümüş nano-disk dizinleri bu amaçla kullanıldı. Yapıların optik karakterizasyonu için geçirim/yansıma ölçümleri yapıldı ve ölçümler zaman düzleminde sonlu farklar yönteminin kullanıldığı simulasyonlar ile desteklendi. Sensörün doğrulaması ilk olarak biotin-avidin sistemi ile yapıldı. Sensör cevabının uygulamanın ardından ilk otuz dakika içinde doyuma ulaştığı gerçek zamanlı ölçümler ile gösterildi. Sensörün derişime bağımlılığı 1 nM-100 nM aralığında gereksinimi karşılayan bir cevap gösterdi. Kırılma indisi duyarlılığı 354 nm/RIU olarak hesaplandı. Son olarak, yöntem ısı tatbiki ile öldürülmüş E.Coli bakterisi tespiti için denendi. Yöntemin bakteri tespitinde de kullanılabileceğine dair umut verici sonuçlar

elde edildi. İkinci olarak, çift rezonans davranışı gösteren, Au-SiO_2-Au katmanların kesik nano-koniler şeklinde uc uca sıralı dizilimi ile oluşan yapıların, YZRS sinyal şiddetini arttırdığı, ilk defa bu çalışmada gösterilmiştir. İyileştirme faktörü hesapları 3.86 $x10^7$ mertebesinde bir sinyal arttırımı olduğunu ortaya koymuştur. Çift rezonanslı tasarım, tek rezonanslı eşleniğinin 10 katı sinyal artışı sağlamıştır. Bu iyileştirmenin yakın infrared-YZRS and yüzeyde zenginleştirilmiş hiper Raman saçılımı (YZHRS) tekniklerinde daha da belirgin bir artış sağlayacağı düşünülmektedir. Bir diğer çalışmada, "eşlenik", dielektrik bir ara halka ile ayrılmış, çift katlı, eş merkezli, periyodik altın halkalardan oluşan SERS alttaşının düz altın filmden 630 kat, aşındırılmış eş merkezli halka yapılarından da 8 kat fazla Raman sinyali artışı sağladığı gösterilmiştir. Bu çalışma içinde $1.67x10^7$ mertebesinde bir iyileştirme faktörü hesaplanmıştır. Son olarak, Metal-Yarıiletken-Metal (MYM) fotodedektörlerin soğurma ve fotoakım toplama performansları, UV dalgaboylarında rezonans gösteren Al nanoparçacıklar sayesinde 1.5 kata kadar iyileştirilmiştir. Bu çalışma ile UV bölgede plazmonik iyileştirme ilk olarak gösterilmiştir. Benzer bir çalışmada yine GaN üzerindeki bir diger MYM dalgaboyu-altı fotodedektörününün performansında, dedektöre eklenen kırınım ağı tasarımı sayesinde resonans dalgaboyunda 8 katlık bir fotoakım artışı sağlanmıştır.

Anahtar sözcükler: Plazmonik, yüzey plazmon polaritonları, nano-parçacık, lokalize yüzey plazmon çınlamaları, Yüzeyde Zenginleştirilmiş Raman Spektroskopisi (YZRS)

Acknowledgement

This thesis would not have been possible without the support of many people.

First and foremost, I would like to express my sincere gratitude to my supervisor Prof. Dr. Ekmel Özbay for his tremendous support, guidance, motivation, encouragement and useful critiques at every stage of this research and also for the exceptional laboratory infrastructure he provided. It was my chance and honor to be part of his research group and gain experience under his menthorship.

I thankfully acknowledge Prof. Dr. Orhan Aytür, Assoc. Prof. Dr.Gülay Ertaş, Asst. Prof. Dr. F. Ömer İlday, and Asst. Prof. Dr. Ali Kemal Okyay for being in my thesis committee and for their valuable time, comments and contributions to my thesis.

I would like to thank Dr. Serkan Bütün for his guidance, tutoring and helps throughout my thesis study. I have learnt a lot from him and our fruitful discussions. I would also like to thank my office mates Damla Ateş and Semih Çakmakyapan. I consider myself lucky to have such easygoing, fun and hardworking friends to share a working day.

I have been blessed with a friendly and hardworking group who offered their excellent cooperation and support at Nanotechnology Research Center throughout my Ph.D. I would like to thank to all the present and former group members but especially to: Dr. Bayram Bütün, Deniz Çalışkan, Cihan Çakır, Adil Burak Turhan, Yasemin Kanlı, Evrim Çolak, Atilla Özgür Çakmak, Hüseyin Çakmak, Engin Aslan, Özgür Kazar, Erkin Ülker, Mustafa Öztürk, Pakize Demirel, Evren Öztekin, Mutlu Gökkavaş, Gökhan Kurt, Basar Bölükbaş, Doğan Yılmaz, Ahmet Akbaş, Dr. Koray Aydın, Dr. Hümeyra Çağlayan and many more.

I also thank to all the faculty members, the graduate assistants with whom I get acquainted at the Department of Electrical and Electronics Engineering.

I would like to take this opportunity to thank to my parents for their endless love, encouragement and moral support throughout my life.

I owe my special thanks to my husband. This thesis wouldn’t exist without his endless love, patience, and support. I dedicate this work to him and our daughter joining us soon. They are the meanings of my life.

Contents

List of Figures

List of Tables

Chapter 1

Introduction

Plasmonics is a major branch of photonics dealing with light-matter interactions in metallic nanostructures [1]. It has become popular since it overcomes the size-compatibility problem present in photonics while surpassing the speed limits in electronics.

Plasmonic devices provide extreme confinement of electromagnetic oscillations to very small volumes beyond diffraction limit at optical frequencies. Applications such as Surface-Enhanced Raman Spectroscopy (SERS) favor the resultant highly intense, concentrated electromagnetic fields [2-4]. Other applications include chemical and biological sensing [5, 6], enhancement of the light trapping properties of thin-film solar cells [7-9], lithography [10-12], microscopy [13], information and communication technologies [14], plasmon waveguides [15], extraordinary transmission through aperture arrays [16] .

Our study focuses on the use of plasmonics, mainly LSPR phenomena, for optical LSPR biosensor design, enhancement of Raman signal in SERS and absorption enhancement in photodetectors.

LSPR is based on the electromagnetic-field enhancement of metallic nanoparticles (NP). The transmission and/or reflection spectrum obtained by illuminating the NPs with light, displays a resonance behavior located at an LSPR wavelength that is related with the NPs' size, size distribution, and shape as well as the type of the metal used and the surrounding environment [17]. LSPR biosensors work on the principle of detecting the refractive index changes of the environment that are induced by the presence of a chemical binding event occurring at the nano-patterned surface and measurement of LSPR wavelength shifts caused by this change [6, 18, 19].

A subcategory that biosensors are used is the detection of food-borne pathogens. Food borne pathogens cause infectious or toxic diseases upon the consumption of contaminated water and/or food. Escherichia coli (E.Coli O157:H7) is among the most serious food borne infections that can cause severe complications and sometimes fatal health problems, particularly among infants, children and the elderly. Traditional methods of bacteria detection like culture collection are effective but time consuming and not very reliable [20]. More rapid methods such as polymerase chain reaction (PCR) and Enzyme linked immunosorbent assay (ELISA) [21-23] require extensive pre-treatment prior to analysis, equipped laboratory and highly trained personnel who can operate the instruments and interpret the results.

On the other hand, Localized Surface Plasmon Resonance (LSPR) systems are easy to manufacture and less expensive, in addition to being portable and practical. Additionally, when LSPR sensors are compared with their closest analog, SPR sensors, working with small samples of analytes is possible and no special geometry (no specific angular conditions of excitation, no needs of prism or grating coupling) for detection is needed.

Both SPR and LSPR sensors rely on detecting small changes in refractive index in the vicinity of a noble metal's surface. Their sensitivities are caused by different mechanisms, but their overall sensitivities are approximately equivalent. SPR sensors exhibit large refractive index sensitivities (2×10^{6} nm.RIU^{-1}) [24, 25]. The LSPR nano sensor, on the other hand, has modest refractive index sensitivity (2×10^{2} nm.RIU^{-1}) [25, 26]. However, the LSPR sensors' enhanced sensitivity is due to the short and tunable characteristic electromagnetic field decay length that is on the order of 5-15 nm, whereas it is on the order of 200-300 nm for SPR sensors [24, 25]. In addition, in SPR systems, there is strong environmental temperature dependency due to the large refractive index sensitivity, whereas LSPR sensors do not require temperature control.

Moreover, SPR sensors require at least a 10×10 μm^2 area for sensing. However, in LSPR sensing, confocal or near-field measurement techniques help minimize the area to a large number of individual sensing elements and even up to a single nanoparticle (NP). Finally, a spectrometer is sufficient to obtain the extinction spectra, so that no complex equipment is necessary [27].

LSPR is highly dependent on the size, shape, and period of the nanoparticles as well as the uniformity of the resultant structure. Chemical patterning methods such as nano sphere lithography (NSL) are usually inexpensive and parallel-natured processes with high throughput. However, only limited shapes and arrays with hexagonal symmetry are feasible. Post deposition steps like thermal annealing or multi angle deposition are necessary for modification in shapes of nanostructures. Moreover, uniform areas are difficult to obtain [28].

EBL, on the other hand, is a modified SEM system that has superior properties compared to other optical or chemical patterning techniques, such as the precise placement and design of arbitrarily shaped NPs with a large selection of geometries of various sizes with fine features. It offers a high resolution of around 10 nm since it is not limited by diffraction limits unlike other optical lithography methods [29, 30]. Therefore, although advanced precision results in a higher cost and greater time, EBL serves academic research and development purposes the best [31, 32].

Surface-Enhanced Raman Scattering (SERS) has been widely studied since its discovery in 1977 [33, 34]. It is a type of vibrational spectroscopy used for the fingerprinting and quantitation of molecular species. It overcomes the inefficiency of Raman spectroscopy and provides highly resolved vibrational information of the Raman-active molecules adsorbed on roughened metallic surfaces. Among its two primary enhancement mechanisms, electromagnetic enhancement, which states that the SER signal is enhanced proportionally to the fourth power of the local electric field intensity [35, 36], is commonly believed

to be more influential than the chemical enhancement based on charge-transfer resonances although the subject is still under debate [37-40].

The nanoscale surface roughnesses serve for the electromagnetic enhancement mechanism via the propagating and/or localized surface plasmons that they support. Classical methods such as oxidation-reduction cycling, use of metal colloids, metal island or cold deposited films result in a heterogeneous distribution of nanoparticles with various sizes, shapes and arrangements. However, nano roughnesses specifically designed by lithographic methods can overcome the unpredictable and irreproducible nature of SERS while increasing the Raman signal intensity [41]. Moreover, this type of controlled fabrication enables the tuning of the plasmon resonances to the desired excitation wavelength [42]. There are numerous reports employing EBL for SERS-active substrate designs with different nanoparticle geometries, particle shapes, sizes, and spatial arrangements yielding high SERS enhancements[41, 43-45].

UV region of the electromagnetic spectrum corresponds to wavelengths under 400nm. UV detectors are used in various commercial civil and military applications such as engine control, space-to-space communications, ozone layer monitoring, UV astronomy, flame/ oil spill/ early missile plume detection. The wide bandgap materials, such as III–V nitrides are widely used for UV detectors for their superior characteristics. GaN is one of the direct, wide bandgap materials with high saturation electron drift velocity. It is radiation hard, resistant to high temperatures and durable for extreme conditions. It is insensitive to visible and IR light that eliminates the need for filtering the long wavelength response and, therefore, intrinsically visible blind. These properties make it an ideal candidate for UV photodetector (PD) applications. GaN-based UV PDs, such as p‑n junction diodes [46, 47], p‑i‑n diodes [48], Schottky barrier detectors [49], and metal‑semiconductor‑metal (MSM) PDs [50] have been reported up to now. Among these structures, MSM PDs offer fabrication simplicity, ultralow intrinsic capacitance and compatibility with planar circuit technology.

In this thesis study, firstly, we demonstrated the use of plasmonic nano-disk arrays for refractive index sensing using LSPR. The idea was applied to the detection of E. Coli bacteria. Secondly, tandem nano-cone arrays were shown to increase the SERS enhancement through the double resonance behavior they exhibit, for the first time in literature. This resulted in more than tenfold higher Raman signals obtained from their single resonance counterparts. Then, a dual layer concentric ring structure was shown to work as an efficient SERS substrate through plasmon coupling between its upper and lower rings. Finally, performance of MSM photodetectors on GaN, working in UV region were shown to increase by 50% with the insertion of Al nanoparticles whose resonances are tuned for UV region, in between the Schottky contacts of the photodetector. This finding was particularly important since the localized plasmons were utilized in UV region for the first time. Similarly, an MSM detector with a sub-wavelength aperture surrounded by an Al nano-structured metal grating was compared to a conventional MSM photodetector employing only a sub-wavelength aperture and eight fold increase in photocurrent enhancement was observed.

1.1 Organization of the Thesis

The organization of the thesis can be summarized as follows: The technical background of the subjects related to the thesis is briefly discussed in Chapter 2. An overview of the surface plasmons and the photodetector basics is provided in this chapter.

In Chapter 3, we present a label-free, optical nano-biosensor based on Localized Surface Plasmon Resonance (LSPR). The design is composed of silver nano-disk arrays located periodically on a sapphire substrate by Electron-Beam Lithography (EBL). Transmission/Reflection measurements were taken for optical characterization and the measurements were verified by finite difference time domain (FDTD) algorithm based simulations. Real time binding and concentration dependency of the sensor structure was studied. The biosensor

design was tested with a biologically complementary biotin-avidin molecule pair and heat-killed Escherichia Coli (E. coli) O157:H7 bacteria.

In Chapter 4, we present our studies on Surface Enhanced Raman Spectroscopy (SERS) utilizing LSPR. In the first part, we present a highly tunable double resonance substrate design to be used in SER measurements. Tandem truncated nano-cones composed of Au-SiO_2-Au layers are designed, simulated and fabricated to obtain resonances at the laser excitation and the Stokes frequencies. SERS experiments are conducted to compare the enhancements obtained from double resonance substrates to those obtained from single resonance, truncated, gold nano-cones. In the second part, a "coupled" concentric ring structure was introduced as a highly efficient SERS substrate and its performance was compared to an "etched" concentric ring structure and plain gold film via SERS experiments. The surface plasmons were imaged with the fluorescence imaging technique and supporting numerical simulations were done.

In Chapter 5, we demonstrate how to utilize LSPR in UV-MSM photodetectors. In the first part, we present an LSPR enhanced MSM UV photodetector on semi-insulating GaN, with plasmonic Al nanoparticles inserted in between its Schottky contacts for an increase in absorption. In the second part, a nano-antenna coupled UV subwavelength photodetector based on GaN is introduced. The design is composed of a subwavelength aperture surrounded by a nano-structured metal grating and compared to a conventional MSM photodetector employing only a subwavelength aperture. The spectral characterizations of the detectors were done through optical transmission measurements. The photodetector characterizations were done through responsivity and I-V measurements.

Chapter 6 is a brief summary of the results, achievements and future directions of the thesis study.

Chapter 2

Theoretical Background

This chapter is a brief description of the important concepts and theoretical aspects related to the thesis work.

2.1 Surface plasmon polaritons

Surface plasmon polaritons (SPPs) are propagating electromagnetic waves bound to the planar metal/insulator interface which decay evanescently perpendicular to the boundary [35]. They arise from the interaction of light with the conduction electrons in metals.

SPPs can be better understood by examining the dispersion relation between the angular frequency (ω) and in-plane wavevector (k) of SPP modes. The SPPs exist at a smooth interface between a dielectric with real and positive dielectric constant $\varepsilon_2 > 0$ and a metal described by a dielectric constant with negative real part $Re[\varepsilon_1] < 0$. For such an interface solution of Maxwell's equations together with the continuity relations for both half spaces result in the dispersion relation as given in Equation (2.1) for the TM mode [35, 51].

$$k_x = \frac{\omega}{c}\left(\frac{\varepsilon_1 \varepsilon_2}{\varepsilon_1 + \varepsilon_2}\right)^{\frac{1}{2}} \tag{2.1}$$

Normally SPPs at a flat metal surface can't be directly excited by an incident plane wave since the dispersion relation lies at right of the light line ($k_x > \omega/c$). In order to excite SPPs, momentum matching is necessary. This can be made possible by the use of a grating or an ATR coupler [51]. In the case of a grating coupler which is also employed in this thesis, the increase of the wavevector necessary for momentum matching is provided by the additional reciprocal lattice vector of the grating and the dispersion relation takes the form:

$$k_x = \frac{w}{c}\sin\theta \pm \frac{2n\pi}{\Lambda} = \frac{w}{c}\sqrt{\frac{\varepsilon_m\,\varepsilon_d}{\varepsilon_m+\varepsilon_d}} = k_{sp} \quad (2.2)$$

Here, "2nπ/Λ" is the reciprocal lattice vector of the grating where "n" is an integer number and "Λ" is the grating period. "θ" is incidence angle of light, "ε_m" and "ε_d"are the dielectric function of the metal and the air, respectively.

The SPP modes on the planar metal surface are bound to and guided by the metal/dielectric interface. They propagate until their energy is dissipated as heat in the metal and their propagation length is given by equation (2.3) [51]:

$$L_i = (2k_x'')^{-1} \quad (2.3)$$

where k_x'' is the imaginary part of the surface plasmon wavenumber.

2.1.1 Localized surface plasmon resonance

Nano-structuring the metal surfaces can be used to control the behavior of surface plasmon-polaritons. When light interacts with metallic subwavelength nanoparticles non-propagating, longitudinal, local plasmon oscillations confined to the metallic nanoparticles called localized surface plasmons (LSPs) are formed. As opposed to the propagating surface plasmons (PSPs), there is no need for phase matching to excite the LSPs.

Physical insight about the origin of LSPs can be gained by analyzing the behavior of a subwavelength spherical nanoparticle in an electromagnetic field under the quasi-static approximation and solving for the Laplace equation for potential. A rigorous analysis is provided in [35] and not repeated here. It turns out that the calculated potential is a superposition of the applied field and a dipole at the particle center with polarizability described in Equation (2.4).

$$\alpha = 4\pi a^3 \frac{\varepsilon-\varepsilon_m}{\varepsilon+2\varepsilon_m} \quad (2.4)$$

Here "α" is the polarizability, "a" is the radius of the nano-sphere, "ε_m" and "ε" are the dielectric constants of the isotropic and non-absorbing medium and the metal, respectively. The most important consequence of this equation is that it implies the presence of a resonance at the so called Fröhlich condition

given in Equation (2.5) given that the imaginary part of the metals' dielectric function is negligible.

$$Re\left[\varepsilon\left(\omega_{sp}\right)\right] = -2\varepsilon_m \tag{2.5}$$

The dependency of the resonance on the surrounding dielectric medium can be further investigated by inserting the Drude definition of metals into Equation 2-2 which eventually shows that the resonance red-shifts as the dielectric constant of the medium is increased. This dependency of the resonance behavior on the surrounding medium forms the basis of the refractive index sensing by metallic nanostructured surfaces.

Note that the quasi-static approximation does not give any insight about the effect of particle size on the spectral position and width of the plasmon resonance. For larger particles comparable to the wavelength of light, one can refer to the Mie theory [52] which is an analytic solution to Maxwell equations for scattering and absorption of electromagnetic radiation by a sphere. Meier et. al.[53] and Kuwata [54] independently derived an expression of polarizability for the first TM mode starting from Mie Theory, given in Equation (2.6) [35].

$$\alpha = \frac{1-(\frac{1}{10})(\varepsilon+\varepsilon_m)x^2+O(x^4)}{(\frac{1}{3}+\frac{\varepsilon_m}{\varepsilon-\varepsilon_m})-\frac{1}{30}(\varepsilon+10\varepsilon_m)x^2-i\frac{4}{3}\pi^2\varepsilon_m^{3/2}\frac{V}{\lambda_0^3}+O(x^4)} \tag{2.6}$$

Here, the term "$x = \pi a/\lambda_0$" is the size parameter and $O(x^4)$ represents the higher order terms. The quadratic terms in the numerator and denominator both cause a shift in plasmon resonance and they explain the retardation effect of the excitation field and the depolarization field, respectively [35]. Inserting Drude definition of metals into Equation (2.6) shows that increase in particle size results in a shift in resonance towards lower energy.

Another version of the Mie equation, that relates extinction (sum of absorption and scattering) to the density and radius of the ordered NP arrays will also be discussed in Section 3.1.7.

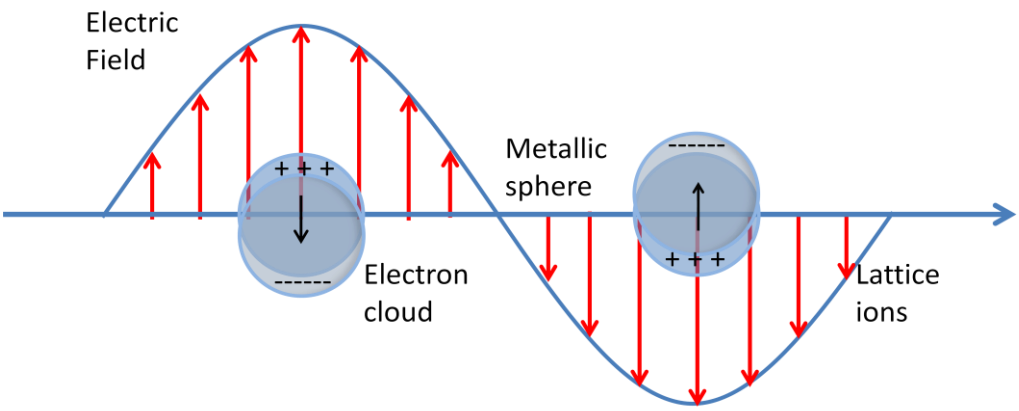

Figure 2.1: Plane wave excitation of a subwavelength metallic spheres depicting localized surface plasmon resonance.

A more qualitative description of the size dependency of the resonance, follows from the plane wave excitation of a subwavelength metallic sphere resulting in the distribution of the unbound conduction electrons and the positive lattice vectors on opposite sides of the surface. (See Figure 2.1) This distribution establishes a restoring force which can be modelled as a mechanical oscillator responsible for the localized surface plasmon oscillations. As the size of the nanoparticle is increased, the seperation between the polarization charges increase. Consequently, the restoring force decreases leading to smaller resonance frequency and, therefore, a red shift in resonance which also follows from the analytic solution [55].

The above mentioned methods are sufficient to gain an insight about the the dependency of the plasmon resonance to the size of the nanoparticles and the surrounding medium. To obtain exact solutions to Maxwell's equations for different geometries, numerical methods such as the finite difference time domain (FDTD) [56] and discrete dipole approximation (DDA) [57] should be employed.

2.1.2 Surface Enhanced Raman Spectroscopy

The discovery of Raman scattering made by Sir C. V. Raman the recipient of the Nobel Prize for Physics in 1930. The observation was that whenever light gets scattered an ordinary diffuse radiation was accompanied by

a scattering with degraded frequency provided that a very powerful illumination was present [58]. However the interest was soon diminished due to the small signal intensity inherent in Raman scattering. After more than 40 years, the research was triggered again by Fleischmann et. al. [59] reporting intense Raman signals from a monolayer of pyridine adsorbed on a roughened silver electrode. The effect was attributed to the increased surface area of the electrodes that would accomodate an increased number of molecules. After this finding, two other research groups independently demonstrated that the associated Raman signals experienced an enhancement factor of 10^5–10^6. Van Duyne et al.[33] attributed the enhancement to an increased electromagnetic field at the roughened surface whereas Albrecht and Creighton [34] asserted the charge transfer mechanism causing a resonance raman scattering. These studies launched the ongoing debate on the origin of SERS and recognized it as a new physical phenomenon with Raman intensity enhancements of 10^5–10^6 for the first time [33, 34]. It is now commonly believed that the electromagnetic mechanism is responsible for the 10^4 enhancement, whereas chemical factors influence on the order of 10-100.

The origin of the SERS enhancement can be better understood by examining the normal Raman scattering which is the inelastic scattering of a photon from a molecule. As a result of the inelastic scattering, the incoming photon energy "$h\upsilon_L$" is shifted by the vibrational energy "$h\upsilon_m$" due to interactions between the photon and the vibrational energy levels of the molecule. If the energy of the scattered radiation is less than the incident radiation, it is called Stokes scattering ($h\upsilon_s = h\upsilon_L - h\upsilon_m$). Otherwise it is called anti-Stokes scattering ($h\upsilon_{as} = h\upsilon_L + h\upsilon_m$). See Figure 2.2. The anti-Stokes line is much less intense than the Stokes line since only molecules that are vibrationally excited prior to irradiation can give rise to the anti-Stokes line. The shift in energy (wavelength) of the scattered light is characteristic to the molecule and provides its chemical and structural information.

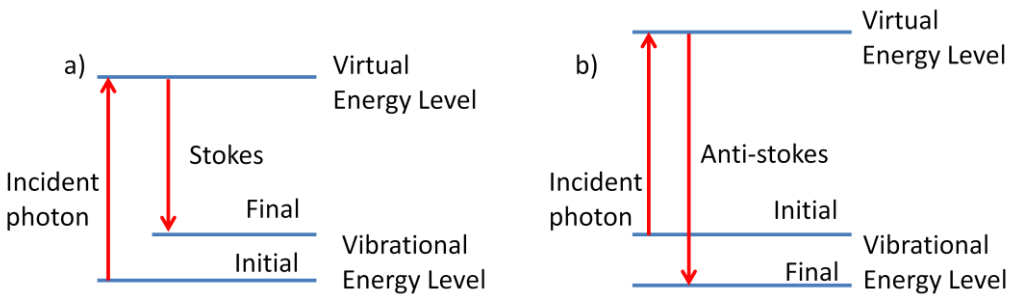

Figure 2.2: Energy level diagram for (a) Stokes scattering (b) anti-Stokes scattering.

Raman is a very weak process since only a small portion of incident photons can contribute. However, there are several mechanisms which can be used to enhance it. The Raman scattering intensity is proportional to the square of the electric field-induced dipole moment, "$\bar{P}$",

$$\bar{P} = \alpha \bar{E} \tag{2.7}$$

where, "α" is the molecular polarizability and "$\bar{E}$" is the electric field incident upon the molecule. Equation (2.7) implies that the Raman intensity can be increased by modifying the molecular polarizability or the electric field experienced by the molecule. "α" can be increased by a charge transfer or a chemical bond formation between the metal and adsorbate. Since such a change would also change the nature of the adsorbate, it is not exactly correct to consider it as a "surface enhancement" effect. This method is considered to serve for the chemical enhancement mechanism. On the other hand, increasing the amplitude of the local electromagnetic field by the generation of localized plasmons on roughened metal surfaces serve for the electromagnetic enhancement mechanism [60].

The origin of the electromagnetic contribution can be understood starting from the expression for power of the inelastically scattered beam $P_s$which can be written as [35],

$$P_s(\upsilon_s) = N\sigma_{SERS}L(\upsilon_L)^2 L(\upsilon_S)^2 I(\upsilon_L) \tag{2.8}$$

where, N is the number of Stokes-active scatterers within the laser spot, σ_{SERS} is scattering cross section for SERS, $I(\upsilon_L)$ is the intensity of the exciting beam and $L(\upsilon)$ is the electromagnetic enhancement factor defined as,

$$L(\upsilon) = |E_{loc}(\upsilon)|/|E_0| \tag{2.9}$$

Here, $|E_{loc}(\upsilon)|$ is the local field amplitude at the Raman active site. Since the frequency difference between the incoming and the scattered photon is smaller than the linewidth of the localized plasmon mode we can consider $|L(\upsilon_L)| \approx |L(\upsilon_S)|$ and end up with the most common enhancement relation [35],

$$R = |E_{loc}|^4/|E_0|^4 \tag{2.10}$$

Equation (2.10) is referred to as the "E^4 enhancement" in literature. It can be stated as the electromagnetic contribution to the total SERS enhancement is proportional to the fourth power of the field enhancement factor. A more rigorous analysis can be found at the works of Kerker and his colleagues [61, 62]. Although the "E^4 enhancement" approximation indicates that for maximum EM enhancement LSPR should match the laser excitation wavelength, in practice it is necessary to achieve electromagnetic enhancement at both the laser and the scattering wavelengths as also stated in Equation (2.8).

Several methods have been used to exploit the relation between LSPR wavelength and SER enhancement. In plasmon-sampled surface-enhanced Raman excitation spectroscopy (PS-SERES) method, samples with different LSPR extinction maxima are illuminated with the same excitation laser and then their respective SERS enhancement factors (EFs) are compared whereas in wavelength-scanned surface-enhanced Raman excitation spectroscopy (WS-SERES) the SER spectra from a single substrate is obtained with the use of many laser excitation wavelengths [63, 64]. Both approaches showed that there is a strong correlation between SERS and LSP resonance. In the work of Haynes [63], the maximum SERS enhancement was reported for excitation frequencies that are slightly blue-shifted with respect to the LSP resonance frequency.

Among the vibrational modes of the molecule under study, the Raman shifted peak closer to the LSP resonance frequency ended with a larger enhancement than that of a farther Raman shifted peak. In the work of McFarland [64], it is stated that the maximum SER EF occurs when the LSP resonance frequency is located in between the excitation and Stokes frequencies so that both the incident photon and the Raman scattered photon are strongly enhanced.

Another idea can be the use of substrates that offer double resonance that can be tuned to the excitation and Stokes frequencies respectively. This idea is implemented and shown to provide a better enhancement than single resonance substrates in Section 4.1.

2.2 MSM Photodetector basics

Photodetectors are devices that convert optical signals into electrical signals. A metal–semiconductor–metal (MSM) photodetector consists of two interdigitated metallic electrodes (Schottky contacts) on the top surface of a semiconductor layer. When an external voltage is applied to the electrodes, one of the Schottky diodes is biased forward and the other in the reverse direction. Incident light in between the electrodes on the semiconductor generates carriers drifted by the electric field. This is a pure drift photocurrent without a diffusion component which would slow down the device response

MSM photodetectors offer several advantages. They are simple to fabricate using a single mask. They have very fast photo-response determined by the saturation velocity of the carriers. There is no need for ohmic contacts which enables low-doped active material. The low capacitance due to the planar geometry results in small RC time constant preferred for high-speed applications. The planar design also enables devices that are IC-compatible.

Quantum efficiency and responsivity are two important properties to characterize a photodetector that are also employed in this thesis. Quantum efficiency can be defined as the ratio of the number of generated electron-hole pairs (EHP) to the number of incident photons as described in Equation (2.11).

$$\eta = \frac{Number\ of\ EHP\ generated}{Number\ of\ incident\ photons} = \frac{I_{ph}/e}{P_0/h\upsilon} \tag{2.11}$$

We can also express quantum efficiency in terms of reflection coefficient of light at the air-semiconductor interface, absorption coefficient (α) and absorptive layer thickness (d) as in Equation (2.12).

$$\eta(\lambda) = (1 - R)\left(1 - e^{-\alpha(\lambda)d}\right) \tag{2.12}$$

Responsivity is the ratio of generated photocurrent to the input optical power and measured in amps per watt (A/W).

$$R = \frac{Photocurrent\ (A)}{Incident\ Optical\ Power\ (W)} = \frac{I_{ph}}{P_0} \tag{2.13}$$

If we relate Equation (2.12) and Equation (2.13) we can express responsivity in terms of quantum efficiency and wavelength as given in Equation (2.14).

$$R = \eta \frac{e}{h\upsilon} = \eta \frac{e\lambda}{hc} = \eta \frac{\lambda}{1.24} \tag{2.14}$$

Chapter 3

Localized Surface Plasmon Resonance (LSPR) Biosensors

We present in this chapter, a label-free, optical nano-biosensor based on the Localized Surface Plasmon Resonance (LSPR) that is observed at the metal-dielectric interface of silver nano-disk arrays located periodically on a sapphire substrate by Electron-Beam Lithography (EBL). The nano-disk array was designed by finite difference time domain (FDTD) algorithm based simulations. Refractive index sensitivity was calculated experimentally as 221-354 nm/RIU for different sized arrays. The sensing mechanism was first tested with a biotin-avidin pair, and then a preliminary trial for sensing heat-killed Escherichia Coli (E. coli) O157:H7 bacteria was done. The results indicate that such a plasmonic structure can be applied to bio-sensing applications and then extended to the detection of specific bacteria species as a fast and low cost alternative.

3.1 EBL designed silver nano- disks used as label free nano-biosensors based on LSPR

This chapter is published as "Electron beam lithography designed silver nano-disks used as label free nano-biosensors based on localized surface plasmon resonance" by Neval Ayşegül Cinel, Serkan Bütün and Ekmel Özbay, Optics Express, vol. 20, issue 3, pp. 2587-2597, January, 2012.

3.1.1 Introduction

Surface plasmons are the electromagnetic waves that exist at metal-dielectric interfaces, caused by the collective motion of valence electrons in the metal. They are named as localized surface plasmons (LSPs) when they are confined to metallic nano scale structures. LSPR wavelength is related with the

NPs' size, size distribution, and shape as well as the type of the metal used and the surrounding environment [17]. It is the sensitivity of LSPR extinction maximum, λ_{max} to the refractive index changes of the local environment induced by a chemical binding event which makes LSPR useful in biosensing experiments [6, 18, 19]. This relation is described in Equation (3.1),

$$\Delta\lambda_{max} = m\Delta n[1 - \exp(-2d/l_d)] \quad (3.1)$$

where, m is the bulk refractive-index response of the NP(s), Δn is the change in refractive index induced by the adsorbate; d is the effective adsorbate layer thickness; and l_d is the characteristic EM-field-decay length [19, 24, 65]. This relationship forms the basis of LSPR wavelength-shift sensing experiments.

In this study, dependency of the LSPR wavelength on the size and period of NPs and the way it can be tuned was shown through simulations and justified by reflection measurements. Surface functionalization was done for biotin-avidin bio-assay and LSPR wavelength-shift sensing experiments were done by transmission measurements. The concentration dependency of the LSPR shifts was observed by changing the analyte concentrations. Real time binding measurements and refractive index sensitivity calculations were made. Finally, the sensor structure was applied and verified to detect E. coli bacteria.

3.1.2 Fabrication

Nanoparticle fabrication starts with the preparation of the sapphire substrate by spin coating PMMA 950 A-2, firstly at 500 rpm for 3 seconds and then at 4000 rpm for 40 seconds. The sample is then prebaked for 90 seconds on a hot plate heated to 180ºC in order to evaporate the solvent in the photo resist and end up with a harder coating. A final step of aqua-save (polymer) coating at 4000 rpm for 40 seconds completes the preparation for EBL. After lithography with the "RAITH E-Line" system, the aqua-save is cleaned with DI water and then the sample is developed at an MIBK:ISO (1:3) developer for 30 seconds. After the development, the sample is cleaned in iso-propanol and blow-dried with nitrogen. The next step is the e-beam evaporation where an Ag coating of

30 nm is carried out in the "Leybold Univex 350 Coating System". After evaporation, the samples are kept in acetone for lift off for 5-10 minutes, and then the excess metal is lifted off with an acetone flush onto the sample with a sterile glass injector. The final samples can be seen in Figure 3.1a and Figure 3.1b. The uniformity of the resultant samples can be seen from the histograms in Figure 3.1c and Figure 3.1d.

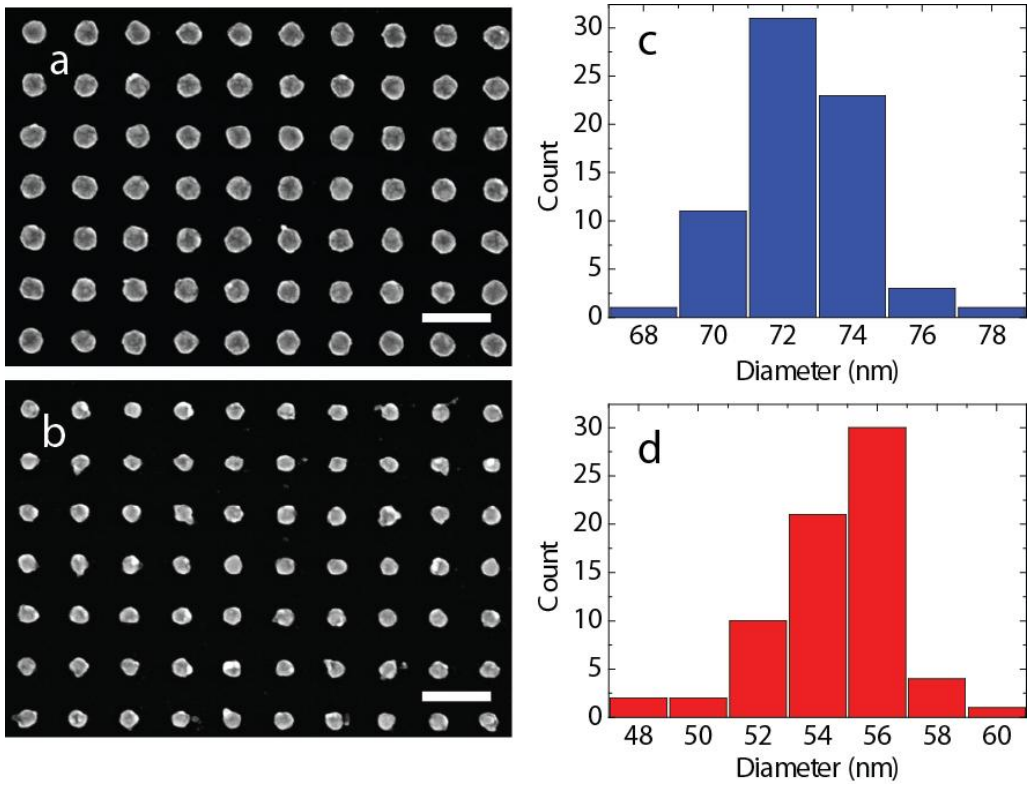

Figure 3.1: SEM images and histograms of EBL fabricated nano-disks. Period 150 nm; EHT is set as 10kV. (a) Diameter of nano-disks is about 73 nm, (b) Diameter of nano-disks is approximately 58 nm. The corresponding histograms are provided in (c) and (d).

3.1.3 Materials and Methods

For this study, Polymethylmethacrylate (PMMA 950 A-2) was used as resist in e-beam lithography. EZ_Link Sulfo-NHS-SS-Biotin (21331) and Avidin (21121) were purchased from Pierce. 11-Amino-1-undecanetiol, hydrochloride [A423-10], and 6-Hydroxy-1-Hexanethiol were purchased from Probior. E. coli O157:H7 Positive Control was purchased from KPL. The package includes heat-killed Escherichia coli O157:H7 cells, at least 3 x 10^9

cfu/mL in dextran solution. It is diluted in a 1/100 ratio, after being rehydrated with 1 mL of reagent quality water. Biotin labeled affinity purified antibody to E. Coli O157:H7 was also purchased from KPL. It is also received in lyophilized pellet form and diluted to 0.5 μg/ml after rehydration with 1 ml of reagent quality water.

3.1.4 Surface functionalization

High affinity chemical pairs are used to test the validity of a biosensor before trials with real antigens and antibodies start. The avidin and biotin (Vitamin H) bioassay is the most extensively studied pair in bio-sensing applications, which is known for one of the strongest non-covalent interactions and their extraordinary affinity towards each other ($K_a=10^{15}M^{-1}$). Biotin is a 244 Da vitamin found in small amounts in all living cells and avidin is a tetrameric protein that is usually found in egg whites [66]. In the current context, the surface functionalization refers to the steps taken for the immobilization of biotin on the Ag nano-disks and, therefore, to be ready to bind with (detect) the avidin in the target analyte. The same procedure is then applied to immobilize biotin labeled antibody and to sense the heat killed E. coli bacteria. Antibody and antigen pairs also have a high affinity towards each other. The use of affinity purified antibody ensures the high specificity for the target antigen and prevents cross-reactivity since they have lower backgrounds and lower nonspecific binding.

The surface functionalization starts by forming a self-assembled alkanethiol monolayer (SAM) on the surface of Ag nano-disks. This is not only necessary for binding biotin to the surface in a well ordered way but also an SAM layer is effective in avoiding the oxidation of Ag nanoparticles in aqueous solutions [67]. This is achieved by mixing 1 mM 11-amino-1-undecanethiol (11-AUT, Dojindo) and 1 mM 6-hydroxy-1-hexanethiol (6-HHT, Dojindo) 2-propanol solutions at a ratio of 1:3 for one hour. Using 6-HHT with 11-AUT reduces the non-specific adsorption and, therefore, increases the stability in the sensor response [68]. To remove nonspecifically adsorbed molecules after the

incubation, the samples were rinsed with deionized water and dried with an N_2 blow after the incubation. Then, for bio-tinylation, 1 mM EZ_Link Sulfo-NHS-SS-Biotin (Pierce, 21331) was covalently linked to 11-AUT for at least three hours. Rinsing with DI water and N_2 blow-drying were repeated [69]. The samples with immobilized biotin were subjected to different concentrations of avidin (Pierce, 21121) solutions, and optical transmission measurements were performed after samples were rinsed and dried.

For the immobilization of biotin labeled affinity purified antibody to E. coli O157:H7), an SAM layer was formed following the same steps as described herein and then the samples were incubated in 0.5 μg/ml of antibody solution for at least 1 hour. E. coli O157:H7 positive control was prepared as described in section 3.1.3 and applied to the sensor surface.

3.1.5 Simulations

The simulations were done to computationally aid the design of nanostructures that give sharp and intense resonances necessary for sensitive detection, and in turn avoiding the labor of fabrication and optical measurements.

The commercial software package "Lumerical", which relies on "Finite-Difference Time-Domain Method" has been used in the simulations. The material data of sapphire and silver were taken from the literature [70]. The mesh sizes were set to values less than or equal to $\lambda/14$, where λ is the source wavelength divided by the refractive index of material of interest. The boundary conditions were set as perfectly matched layer (PML) in the direction of illumination for eliminating the undesired reflections from boundaries and periodic in the perpendicular plane for simulating a single unit cell and thereby saving simulation time. Numerical stability is ensured by setting the time step less than 0.02 fs based on the chosen mesh sizes.

Two sets of simulations were carried out to see the effect of changes in the period and diameter of nano-disks. In the first set of simulations, radii and

the heights are held constant at 30 nm, and the period was varied 150-300 nm. The increase of the period without a change in radius, leads to a decrease in the density of the nanostructures and thereby a decrease in resonance intensity. See Figure 3.2a. In the second set of simulations, the period was held constant at 150 nm, height at 30 nm, and the diameter was varied between 30-73 nm. The increase in radius resulted in a red shift in the resonance wavelength and an increase in the intensity of the resonance wavelength. See Figure 3.2b.

Simulation results and reflection measurements are in good accordance, which can be seen from a direct comparison of Figure 3.2b and Figure 3.2c. Any discrepancy may be attributed to the differences in the material data and physical dimensions used at the simulations and the fabricated design.

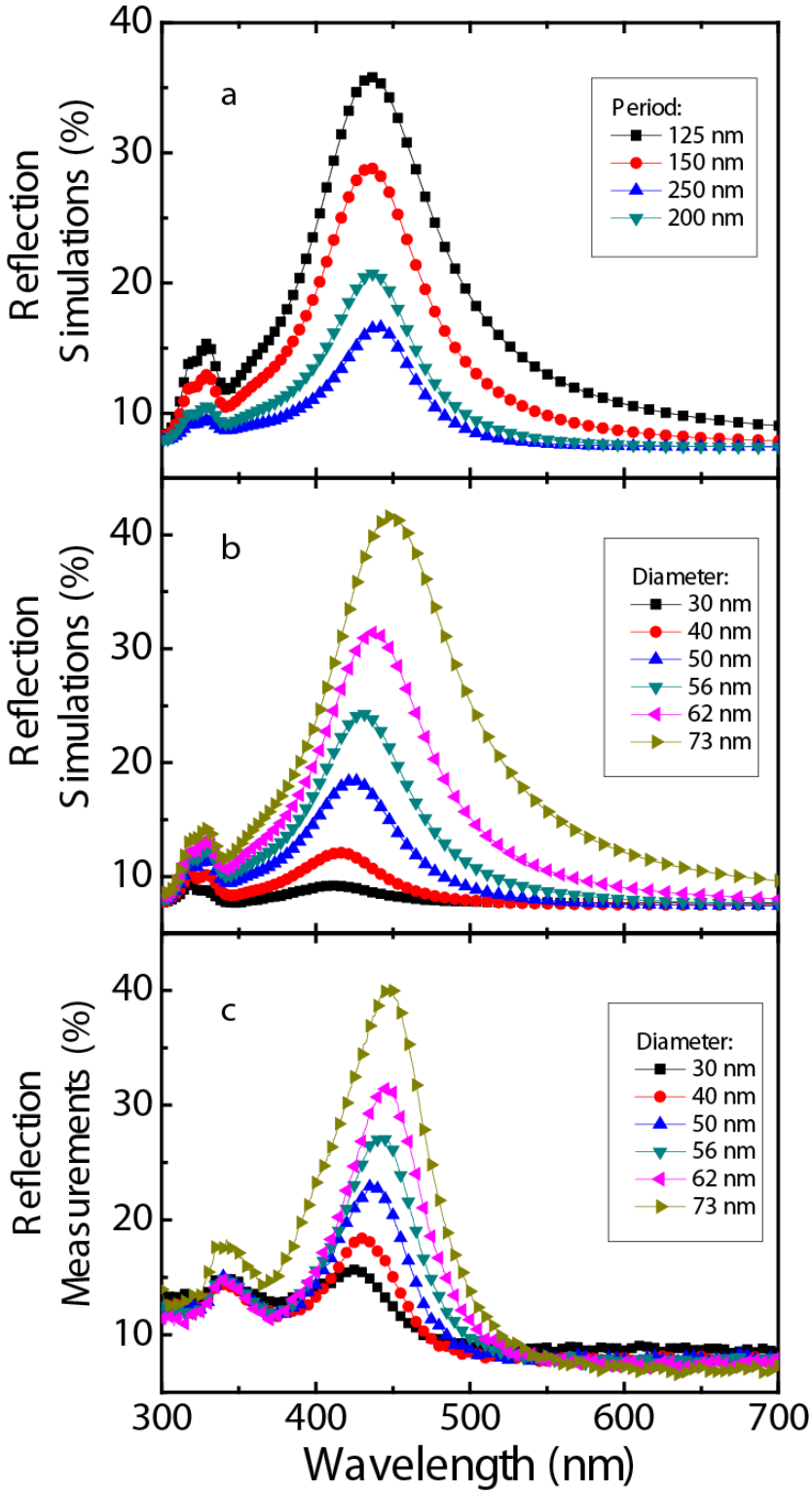

Figure 3.2: Simulations versus measurements. (a) Reflection simulations: Radii and the height are held constant at 30 nm, and periods vary 150-300 nm. (b) Reflection simulations: Periods held constant at 150 nm, height is 30 nm, and the diameter varies 30-73 nm. (c) Reflection measurements: Periods held constant at 150 nm, height is 30 nm, and the diameter varies 30-73 nm.

3.1.6 Measurements

A custom-made optical set-up has been used for the transmission measurements of the samples. The set-up is basically comprised of a spectrometer (OceanOptics-USB4000), a personal computer (PC), and a Xenon light source (Spectral Products ASB-XE-175). Light is transmitted by a multimode optical fiber to a lens that illuminates the biosensor through a collimating lens that collects the light at the input. The light is then transmitted through the biosensor and collected by the imaging lens. The image is projected onto an aperture that enables only the signal from the selected region on the sample being measured to be transmitted. Another focusing lens couples this signal to the collection fiber. The spectrum is then measured by the spectrometer. The set-up is described schematically in Figure 3.3.

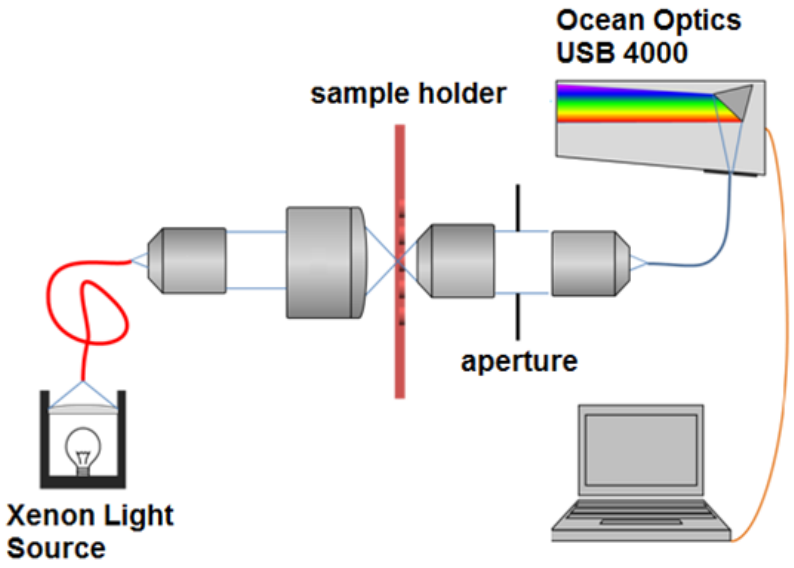

Figure 3.3: Schematic depiction of custom spectral transmission set-up.

In reflection measurements, we used a similar set-up composed of a personal computer, a spectrometer (Horiba Jobin Yvon-Triax 550) equipped with a CCD (Horiba Jobin Yvon-Symphony), a broad spectrum Xenon light source (Spectral Products ASB-XE-175), and a microscope with a moving stage

and camera (Olympus). Light from the Xenon source was coupled to the microscope, through an optical fiber ended with a collimator, and focused onto the sample through the microscope. The light reflected from the sample is collected back with the microscope objective. The collected light is fed into the spectrometer for the reflectance measurements.

Three measurements are taken to obtain the respective spectrum: one to measure the total reflected/transmitted light, second to measure the background error due to losses in the optical path and the third to obtain the reflected/transmitted light from the nano-disk arrays. The reflectance/transmittance is the ratio of the sample light intensity to reference light intensity, where background noise is subtracted from both measurements separately. Similar measurement schemes are available from the literature [6, 19, 71].

Graphs showing the reflection with respect to the wavelength can be seen from Figure 3.2c. The transmission measurements taken from the bio samples at every step of the surface functionalization are shown in Figure 3.4.

3.1.7 Results and Discussion

In this study, silver nano-disks on sapphire substrate are used as a sensor platform. Silver is selected since it has sharper and more intense LSPR than gold [72]. The chemical instability and oxidation issue of silver is overcome by designing a vacuum box to keep the samples in between measurements and fabrication steps. Sapphire is transparent at optical frequencies which makes it suitable for reflection and transmission measurements. And the dimensions are selected to keep the operation at around 400-500 nm. By this way it is guaranteed to stay at optical frequencies after surface modification steps that cause red shift. This will gain more importance in future studies that involve the detection of real pathogenic bacteria where more complicated surface functionalization may be necessary since working at this portion of the spectrum provides a means for gentle detection that does not destroy the structure of matter [73].

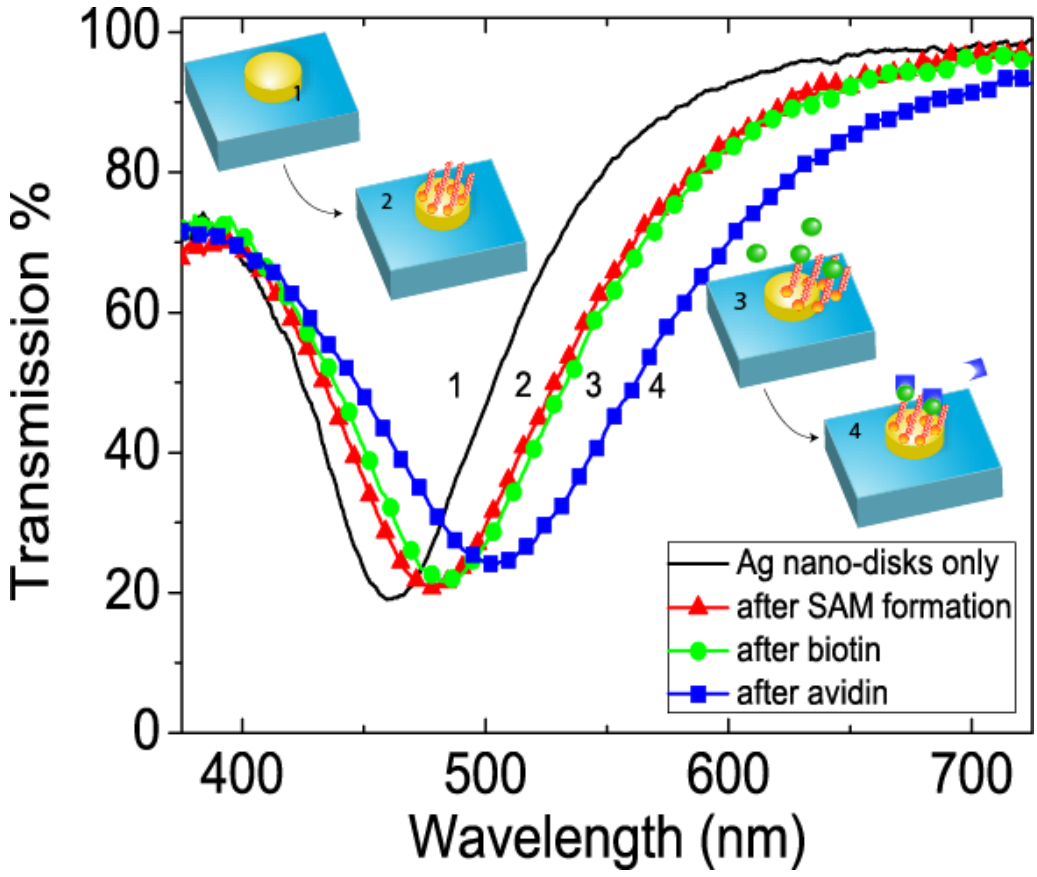

Figure 3.4: Transmission measurements for silver nano-disks before application of chemicals (1), after the application of chemicals (2), after the application of biotin (3), and after the application of avidin (4). Inset: the schematic illustration of surface functionalization steps.

The first set of simulations and reflection measurements are in good correlation as can be seen in Figure 3.2. In both, the increase in radius resulted in a red shift in the resonance wavelength and an increase in intensity of the resonance. Mie theory may help explaining these results. Although Mie theory is originally developed for describing the scattering properties of spherical nanoparticles, it is frequently used in getting an intuition about LSPR shifts in other geometries, too [74]. In Mie Theory, extinction (sum of absorption and scattering) is directly proportional with the density and cube of radius of the nanostructures. (See Eq. (3.2) below).

$$E(\lambda) = \frac{24\pi N_A r^3 \varepsilon_m^{3/2}}{\lambda \ln(10)} \left[\frac{\varepsilon_i(\lambda)}{(\varepsilon_r(\lambda)+2\varepsilon_m)^2+\varepsilon_i^2(\lambda)} \right] \quad (3.2)$$

Here, "λ" is the radiation wavelength and "E(λ)" is the extinction. "N_A" is the areal density and "r" is the radius of the nanoparticles. "ε_m" is the dielectric constant of the medium surrounding the metallic nanoparticles. "ε_i" is the imaginary portion and "ε_r" is the real portion of the metallic nanoparticles' dielectric function.

When Mie theory is correlated with our first case (Figure 3.2a) the increase of the period without a change in radius leads to a decrease in the density of the nanostructures. According to Mie Theory, this should lead to a decrease in reflection intensity, which is the case in the simulations where increasing the period led to a decrease in the amplitude of intensity.

In the second case (Figure 3.2b), the increase in radius keeping the period constant is expected to increase the areal density of nanoparticles as well as the amplitude of resonance intensity that is fulfilled in both the simulations and measurements (Figure 3.2b-c). The size dependency of the LSPR shifts is already discussed in section 2.1.1 on another version of Mie formulation. Increase in size is expected to result in a red shift in resonance wavelength as a consequence of this formulation. This is also the case in both the simulations and measurements. Since the equation is derived for spherical geometry, the dependence of LSPR shifts on the shape and the height is not very explicit.

Transmission measurements were performed after every step of surface functionalization to verify their success. Figure 3.4 depicts the LSPR wavelength shifts for the Ag nano-disks of the period 150 nm, height 30 nm, and diameter 60 nm. After the formation of SAM, the application of biotin and avidin; 16 nm, 8 nm, 20 nm red-shifts were observed, respectively. These amounts of shifts are reasonable and sufficient to show that the binding events take place and the sensor has detected the applied material without any uncertainty.

An important feature of biosensors is their ability to determine the concentration of the analyte to be detected. Experiments have been conducted to verify that the designed sensor has different responses at different analyte

concentrations and the measurements taken showed that the sensor has an adequate response at the 1 nM-100 nM range, which can be fitted to a sigmoidal curve as shown in Figure 3.5. Sigmoidal curves are used for describing the specific binding of bio-molecules due to the nature of binding [27, 65, 68, 69]. As the concentration of the analyte increases, the surface-receptors, namely biotin bound to the SAM formation on Ag nano-disks, start to saturate. The sigmoidal fit justifies the saturation as well as the steric hindrance effects that are expected as the concentration of the analyte increases.

Another experiment was conducted to see the real time binding, after the application of avidin. The measurements showed that the greatest response was observed shortly after the application of avidin within the first few minutes and the response was well saturated within half an hour. This experiment showed that the designed LSPR sensor has a fast response enabling real time detection, which is a very important feature for biosensors where the need of detection is urgent. The real time binding measurement results are provided in the inset of Figure 3.5.

After the verification of the sensor structure with a biotin-avidin pair, another trial with heat-killed E. coli was conducted. Since active E. coli bacteria can only be studied in BL2 (biosafety level 2) laboratories [75], heat-killed, potentially harmless positive controls were used in order to test the sensor structure [76]. The samples with immobilized antibody were subjected to a heat killed E. coli bacteria solution, and the transmission measurements were performed after rinsing and drying. To check for the repeatability of the results, a second measurement was taken after a second incubation of the sensor with the same bacteria solution. The results show that there is a red-shift of 4.5 nm

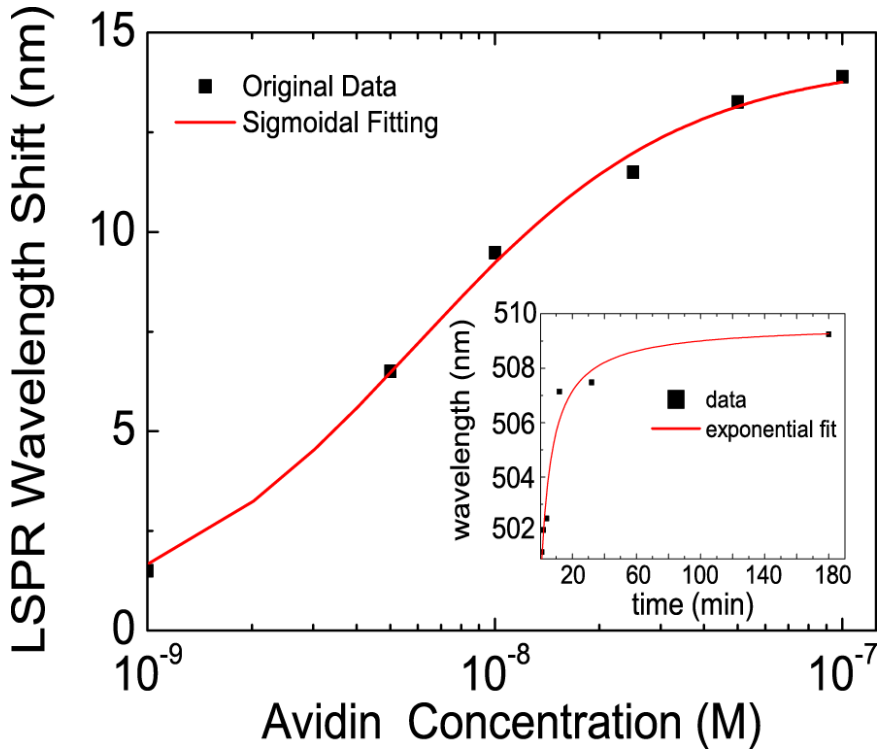

Figure 3.5: LSPR wavelength shifts with respect to avidin concentration. A sigmoidal dependence was observed and fit by hill function (red curve; inflection point slope ~ 0.99). Inset: Real time binding, LSPR wavelength versus time after the application of avidin is shown. Real time measurements after 1 minute, 2, 4, 12, 32 minutes and 3 hours are taken.

after the application of bacteria and this measurement is stable and repeatable (Figure 3.6). For the time being, this trial only shows the possibility of such a sensing method. Specificity and concentration dependency should be studied before calling the sensor an E. coli sensor. A limit of detection study is not done yet. However, our current E. coli detection concentration of ~10^7 cfu/ml is comparable to the direct assay detection limit of 10^6 cfu/ml for a surface plasmon immunosensor for the detection of E. coli although it is much smaller than the sandwich assay detection limit of 10^3 cfu/ml for the same sensor [77]. It should be noted that no optimization studies have been performed yet, so there is still room for improvement.

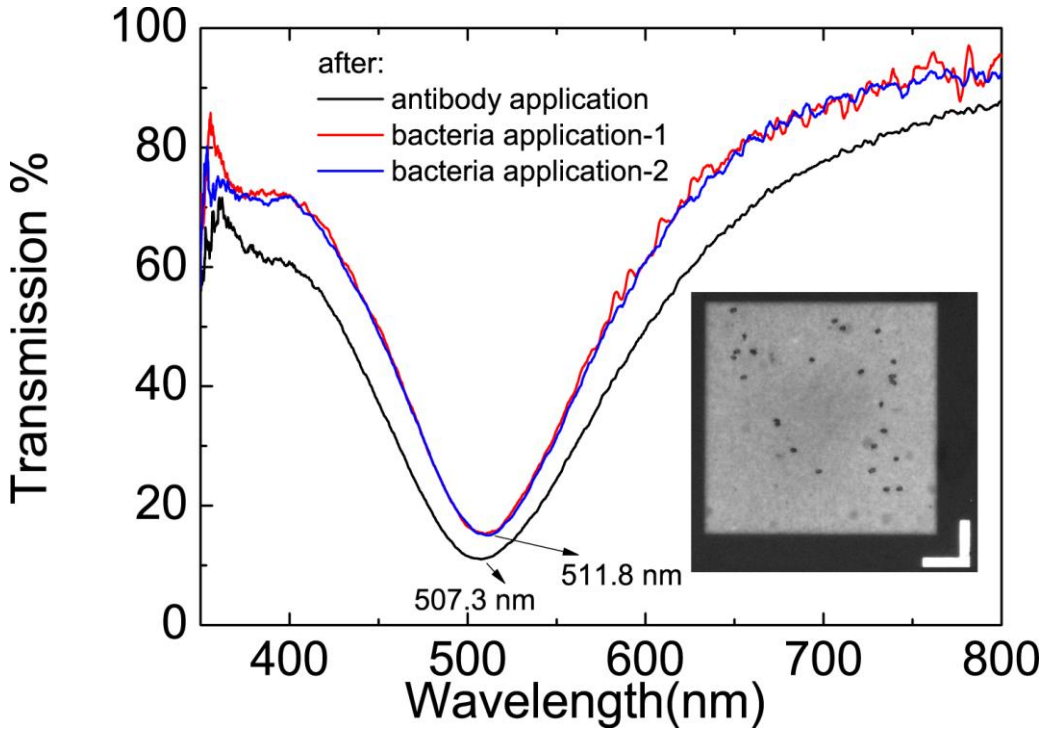

Figure 3.6: Transmission measurements after incubation in antibody and E. coli positive control solutions. inset: Dark-field Electron-microscope image of the sensor surface after the bacteria is applied. The applied bacteria look like cylindrical rods. The square shaped sensor area is 50um x 50um.

An important feature of biosensors is refractive index sensitivity, which can be defined as the response of the resonance peak wavelength to changes in the bulk refractive index of the surrounding environment. In this study, we obtained the refractive index sensitivity through calculations based on transmission measurements. The sensors are exposed to iso-propanol (n=1.3776) and water (n=1.3325) and transmission measurements were taken while the samples were incubated in the solutions. The refractive index sensitivity was then calculated using the peak resonance wavelengths obtained through the transmission measurements using the formula $\Delta\lambda/\Delta n$; where Δn is the change in the refractive index of the dielectric environment and Δλ is the experimentally measured shift in the peak resonance wavelength. A refractive index sensitivity value of 221 nm/RIU was obtained for 40 nm diameter silver nano-disks and 354 nm/RIU for 80 nm nano-disks both with period 150 nm. These values are

comparable to those obtained in the literature for different types of LSPR sensors that range between 191 and 366 nm/RIU [26, 71, 78-81].

Another important comparative parameter of sensing devices is the figure of merit $FOM = (\Delta\lambda/\Delta n).(1/\Delta\omega)$, where Δω is the FWHM (full-width at half-maximum) of the resonant dip. This parameter figures out the ability of the sensor to accurately measure small changes in the resonance wavelength considering the sharpness of the resonance behavior. Although there is an improvement in the sensitivity factor with the increase in diameter, FOMs calculated for the two cases described above are close to each other: 2.33 and 2.81 since the FWHM increases from 95 nm to 126 nm as the diameter increases. In the experimental trials we have chosen 60 nm diameter nanoparticles for their good sensitivity and moderate FWHM values considering the above calculations.

3.1.8 Conclusion

In this study, EBL designed silver nano-disks are shown to be used as label free nano-biosensors based on LSPR and verification is done through simulations and optical measurements.

Simulations are important since they can avoid unnecessary fabrications especially when the structure has to be tuned to a desired wavelength. In many other fabrication techniques, LSPR substrates are hardly repeatable and the resultant sizes are not predictable so that the structure has to be fabricated to gain an intuition about the resonance frequency [67, 69].

It is possible to extend the detection of heat killed E. coli bacteria for the detection of other pathogenic bacteria since biotin is capable of being conjugated to many proteins without altering their biological activity. If biotin conjugated antibody of specific bacteria is immobilized onto the sensor then similar steps can be taken to detect the presence of its antigen in target solution. By this method, one can even achieve multi-output sensor chips that can detect several types of bacteria simultaneously.

Future study includes examining the concentration dependency, specificity, reversibility, selectivity, and optimization of the sensor. The detection of bacteria in solutions, food, and biological and medical samples and the design of a handheld, portable device comprising its own light source, spectrometer, and sample holder is the next step. The technique can then be used in the continuous monitoring of food and water supplies, to protect against terrorist attacks, or speed up the identification of the species when time is of essence for medical treatment.

Chapter 4

Efficient Substrate Designs for Surface Enhanced Raman Spectroscopy

In this part of the thesis, we propose highly efficient substrate designs to be used in SERS.

In the first part of the chapter, we propose a tunable double resonance substrate design. Tandem truncated nano-cones composed of Au-SiO_2-Au layers are designed, simulated and fabricated to obtain resonances at the laser excitation and the Stokes frequencies. SERS experiments are conducted to compare the enhancements obtained from double resonance substrates to those obtained from single resonance gold truncated nano-cones. The best enhancement factor (EF) obtained using the new design is 3.86×10^7.

In the second part of the chapter, a "coupled" concentric ring structure has been designed, fabricated, tuned, and compared to an "etched" concentric ring structure and plain gold film via SERS experiments. The proposed design gives Raman signal intensity 630 times larger than plain gold film and 8 times larger than an "etched" concentric ring structure. The EF is calculated as 1.67×10^7 for the coupled-concentric ring structures. The surface plasmons were imaged with the fluorescence imaging technique and supporting numerical simulations were done.

4.1 "Fairy Chimney"-Shaped Tandem Metamaterials as Double Resonance SERS Substrates

This section of the thesis is accepted by "Small" under the heading "Fairy Chimney Shaped Tandem Metamaterials as Double Resonance SERS Substrates" by Neval A. Cinel, Serkan Bütün, Gülay Ertaş, Ekmel Özbay, to be published in 2013.

4.1.1 Introduction

SERS EF is influenced from the particle near-field enhancement at the incident (excitation) wavelength and the re-radiation of the Raman signal emitted at the near field of the nanostructures at Stokes wavelength [82, 83]. Therefore, double resonance designs can provide increased enhancement when the resonances are properly tuned to the excitation and the Stokes frequencies respectively. This can be summarized using Equation (4.1). Here, E_{loc} and E_0 stands for the local and the incident electric fields, respectively. λ_{exc} refers to excitation wavelength and λ_{stokes} is the Stokes wavelength [84].

$$G_{SERS} \propto \left|\frac{E_{loc}(\lambda_{exc})E_{loc}(\lambda_{stokes})}{E_0(\lambda_{exc})E_0(\lambda_{stokes})}\right|^2 = g(\lambda_{exc})g(\lambda_{stokes}) \qquad (4.1)$$

Recently, there have been some reports that investigate the double resonance structures as SERS substrates [85, 86]. In the work of Chu [85], the design includes a metallic nano-disk array separated from a gold film by a dielectric spacer. The surface plasmon polariton on the gold film interacts with the LSPR of the metallic array and double resonance characteristics is observed in optical transmission measurements. In the work of Banaee [86], "in-plane" nano-particle pairs are used to obtain the plasmonic coupling. In the current study, we propose a different way to achieve plasmonic coupling by aligning the nanostructures in the light propagation direction which would end up with a better spatial overlap. Tandem Au-SiO_2-Au truncated nano-cones designed this

way, offer a highly tunable means to obtain the desired resonance frequencies. Their transmission spectra exhibit two separate and tunable transmission dips associated with hybridized modes resulting from the dipolar coupling between the metallic layers split with a dielectric spacer. Similar tandem metamaterial structures reported in literature include 2D arrays of Al-Al_2O_3-Al nanoparticle pairs and Au-MgF_2-Au nanoparticle pairs on quartz substrates fabricated using extreme-UV interference lithography (EUV-IL) [87, 88]. However their strong near-field coupling is shown to increase SERS enhancement firstly in this study. The best SERS EF obtained from tandem double resonance substrates in this study is in the same order with the work of Chu [85]. Double resonance substrates provided a roughly 10 fold increase in EF than their single resonance counter-parts.

4.1.2 Fabrication and Design

The SERS-active roughened surfaces can be fabricated by several methods like oxidation-reduction cycling, metal colloids, cold deposited films, island films and lithography. Since LSPR is highly dependent on the size and shape of the nano-particles, lithographically prepared surfaces provide the most predictable and reproducible substrates whose resonances can be tuned easily [40]. Lithographically prepared nano structure designs can also be simulated accurately which reduces fabrication efforts. The enhancement factor calculation is more reliable due to more accurate estimations of physical dimensions, too. In this study we have fabricated our SERS-active substrates using electron beam lithography which produces highly reproducible nano-particle arrays with uniform shapes and size distributions [42].

For fabrication, an optically transparent sapphire substrate was chosen since transmission measurements were planned for optical characterization. The sapphire substrate is spin coated with Poly(methylmethacrylate) (PMMA 950 A-2) at 4000 rpm for 40 seconds. After pre-bake for 90 seconds at 180ºC, aqua-save (polymer) coating is done using the same parameters. “RAITH E-Line” system is used for lithography. The sample is developed at 1:3 MIBK:IPA

(Methyl Isobutyl Ketone: Isopropyl Alcohol) developer for 40 seconds. The metal coating is done in "Leybold Univex 350 Coating System". The samples are kept in acetone for lift off for 5 minutes, and then the excess metal is lifted off with acetone flush.

The substrate is composed of several sensor areas of 50 μm x 50 μm that contains different sized nano-arrays. The sizes of individual nano-particles are varied by changing the exposure dose of electron beam. Due to the self shadowing effect during metal-evaporation the nanostructures are shaped into truncated cones. The resultant shapes resembles and named after "Fairy Chimneys" rock formations found in Cappadocia, Turkey [89]. The size, shape and period of the nano-particles are investigated by scanning electron microscope (SEM). The cone angle is determined as $\theta \sim 20° \pm 2°$. The period of the resultant arrays are 200 nm, radii ranges from 35 nm to 60 nm. The metal thicknesses are 30 nm-15 nm-30 nm for Au-SiO_2-Au layers, respectively. The SEM images taken from various sensor areas are shown in Figure 4.1a-b.

For comparison of Au-SiO_2-Au tandem structures exhibiting double resonance behavior to gold structures exhibiting single resonance behavior another sample is prepared following the same procedure as described above. The sensor areas that have their resonance at the same wavelength with the electrical resonance of double resonance structures are selected for comparison.

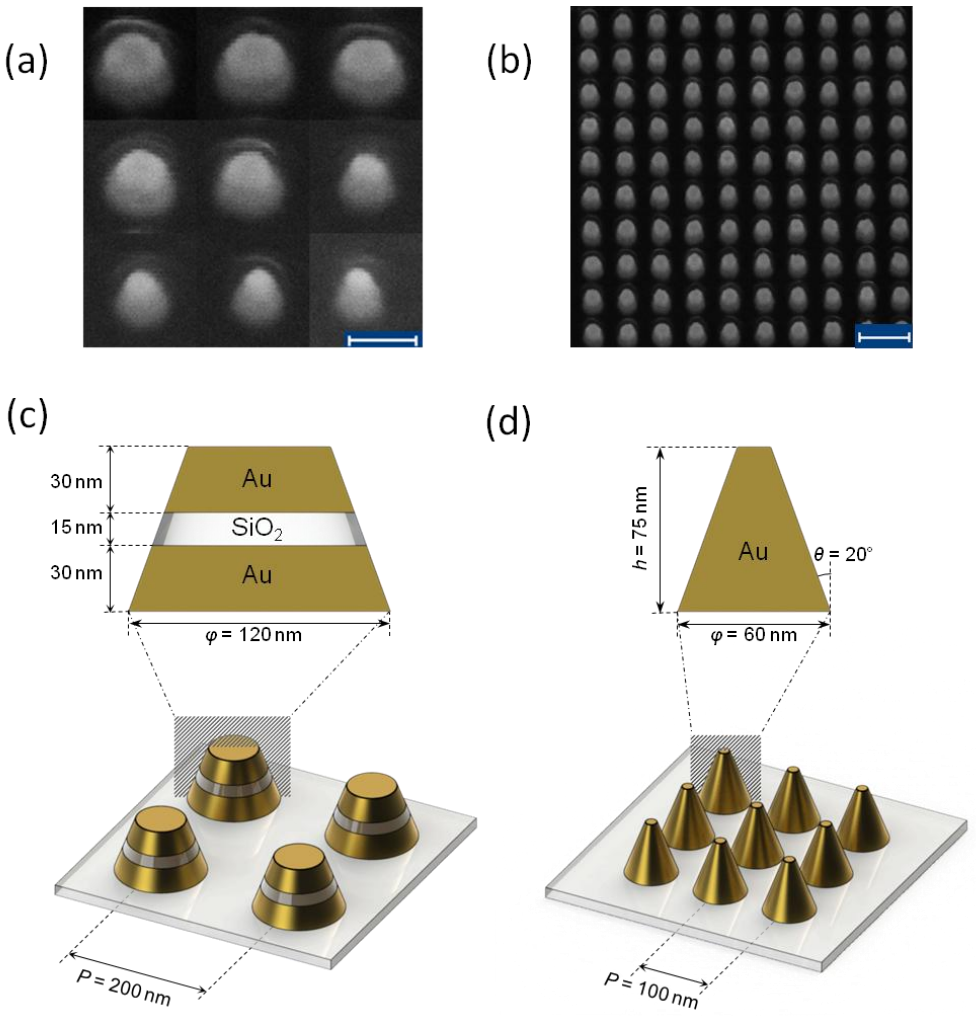

Figure 4.1: (a) The SEM images taken at 45 degrees angle. A single nano-particle from different arrays with the same period but different radii changing from 35-60 nm is collaged to give insight about the variation of the geometrical shapes with the applied dose. The scale bar is 100 nm (b) 60nm radius array with period 200nm. The scale bar is 300 nm. (c) "Tandem" nanostructures (d) "Only gold" nanostructures

4.1.3 Optical Transmission Measurements

The optical characteristics of the tandem structures are studied using the custom spectral transmission setup described in Section 3.1.6, Figure 3.3. To obtain the optical transmission characteristics, background light intensity is firstly measured with the light source off. Then, reference light intensity is measured with the light source on for an empty reference point, which means from the sapphire substrate with no nano-cones. Finally, the sample light

intensity is measured as transmitted light at the presence of the nano-cone arrays under perpendicular illumination. The transmittance is the ratio of the sample light intensity to reference light intensity, where background noise is subtracted from both measurements. The measurement results are presented in a along with the simulation results in b.

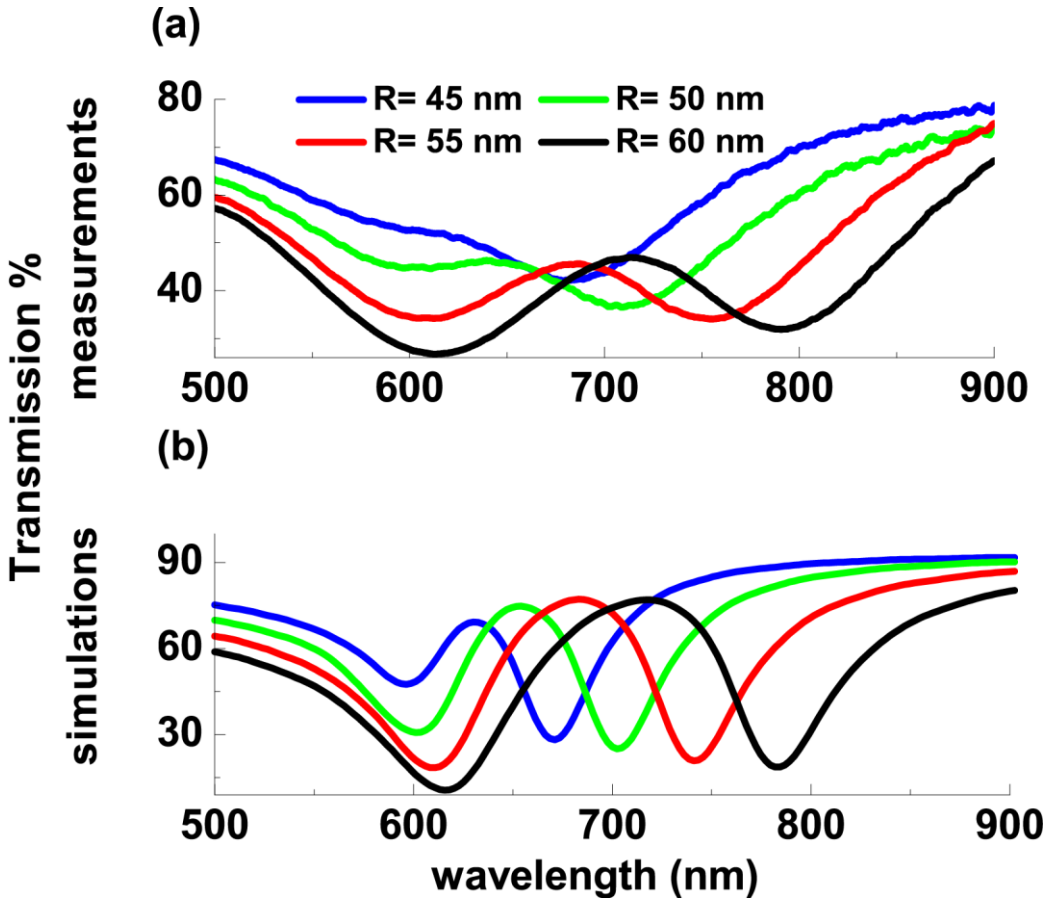

Figure 4.2: (a) Transmission measurements for the truncated nano-cones. Period is 200 nm. Bottom radius vary from 45-60 nm, respective heights of the Au-SiO_2-Au layers are 30-15-30 nm. (b) Simulation results for the similar sized arrays

4.1.4 SERS and Raman Experiments

The SERS data is collected by Horiba LABRAM Raman Spectrometer. The He-Ne excitation laser is 632.8 nm. The data is collected with 100X objective with 0.9 numerical aperture. The calculated spot size for the used objective is around 0.8 μm. Slit size of 200 μm and hole size of 1100 μm is used

throughout the measurements. The data is collected with the same accumulation and exposure times for all samples.

Benzenethiol is purchased from Sigma-Aldrich and used as is in the Raman experiments. The substrates for SERS experiments are prepared by spin coating benzenethiol (10 mM) solution in ethanol, at 4000 rpm for 40 seconds. This provides a homogenous coating of the molecule on the different sensor areas residing at the middle of the same substrate.

4.1.5 FDTD Simulations

3-D simulations are carried out on a single unit cell of the different sized arrays with a commercial "Finite-Difference Time-Domain Method" solver "Lumerical". The material data of Au is taken from the work of Johnson and Christy and for SiO_2 and sapphire from the work of Palik [70, 90]. The truncated nano-cones are illuminated by normal incidence from air side by a plane wave of wavelength range 500-900 nm. The dimensions of the nanostructures are chosen in accordance with the physical sizes measured with SEM. The bottom radii of the truncated cones range from 45-60 nm whereas the heights are 30-15-30 nm for Au-SiO_2-Au layers respectively. Period is 200 nm and the cone angle is taken as 20°. The boundary conditions were set as perfectly matched layer (PML) in the direction of illumination to prevent undesired reflections from boundaries and periodic perpendicular to the direction of propagation. A mesh override region covering the nanostructures is used for fine resolution with high accuracy. The mesh sizes are set to 2nm for transmission simulations whereas finer mesh sizes up to 0.25 nm is used for cross sectional monitors that depict E-field distributions.

The simulations are in agreement with the optical measurements in terms of resonance frequencies. The peaks at the shorter wavelengths have electric dipolar nature and is referred as electrical resonance whereas the peaks at the longer wavelengths have magnetic dipolar nature and referred as magnetic resonance [88]. Experimental data suffers from broadening due to possible

fabrication imperfections such as size and/or shape dispersions however the positions of the resonance dips are closely matched.

It can be seen that the electrical resonances are not influenced much from diameter change at a fixed SiO_2 spacer thickness. However the magnetic resonance can be tuned by varying bottom radii as can be seen from Figure 4.3. In SERS experiments usually a fixed wavelength laser is available and used for different molecules each exhibiting Stokes shifted Raman lines at different wavelengths. Such a design can aid to fix electrical resonance at the desired excitation wavelength and tune the other to match the tracked Raman line of the molecule under study. Such a tuning is possible by varying spacer thickness, too [88].

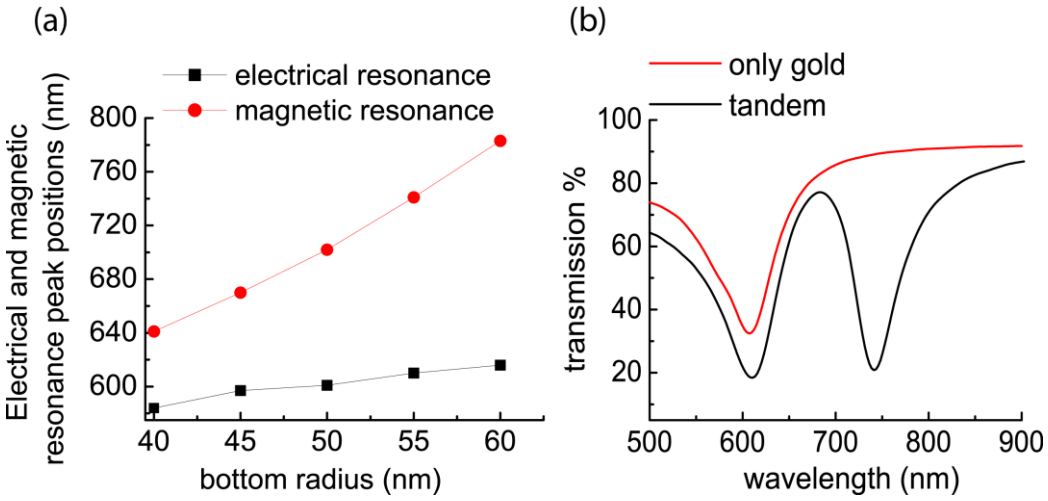

Figure 4.3: (a) The variation of electrical and magnetic resonance peak positions with changes in bottom radius. Magnetic resonance is prone to changes in physical dimensions whereas the electrical resonance is not very sensitive. (b) Simulated transmission spectra of the tandem and gold truncated nano cones used for comparison. Physical dimensions are illustrated in Figure 4.1c and Figure 4.1d.

For performance comparison gold truncated nano-cones that have single resonance wavelength matched with the electrical resonance of tandem structures are simulated in accordance with the fabricated structures' dimensions. Their respective transmission spectra are shown in Figure 4.3b. The E-field distributions are drawn for both cases at the experimental excitation wavelength at 632 nm and at the tracked Raman line of benzenethiol under this

illumination at 785 nm. Double resonance structures exhibit a higher E-field intensity at both wavelengths in "hot-spots" formed at metal-dielectric boundaries. On the other hand, single resonance gold structures exhibit poor E-field intensity at the Stokes shifted Raman line far from its resonance wavelength. This can be followed from the cross sectional electric field distributions provided in Figure 4.4. The figures also depict the spatial overlap of the enhanced fields for tandem structures at the two wavelengths that increases $|E_{exc}|^2 \cdot |E_{stokes}|^2$ and therefore the total electric field intensity.

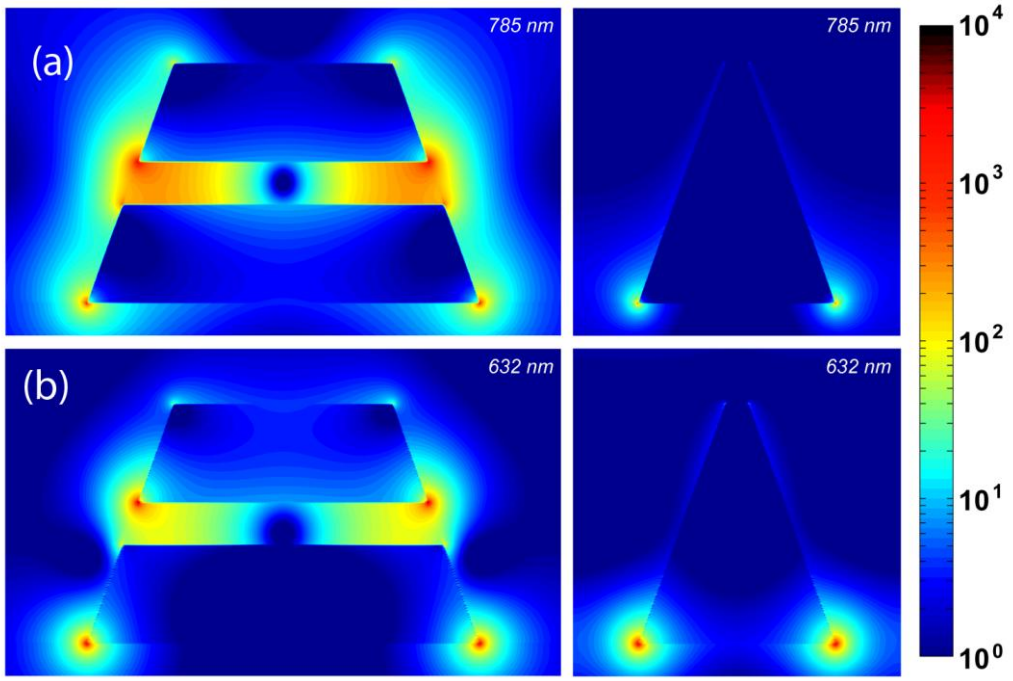

Figure 4.4: Cross sectional electric field distributions (log (|E|2)) of double and single resonance structures where the resonance of gold nanoparticles match the electrical resonance of tandem nanostructures. a) at raman shifted wavelength of tracked Raman line (785 nm) b) at excitation wavelength (632 nm). The dimensions are the same as indicated in Figure 4.1c and Figure 4.1d.

The electromagnetic enhancement mechanism that is responsible for most of the resultant SERS enhancement relies on the intensity of the local electric field. Another simulation is done for the comparison of the electric field enhancements keeping all the previous settings. The electric field distribution is obtained for both cases at excitation and Stokes shifted wavelengths by 3D monitors. Then $|E_{exc}|^2 \cdot |E_{stokes}|^2$ is integrated over the exposed volume and

normalized with the total surface area. The results for "tandem" structures with bottom disk radius of 60 nm and 50 nm are then compared with "only gold" structures with 30 nm radius at the same total height, in order to correlate with the SERS experiments. The resultant enhancement is about 16 fold for 60 nm radius array for the Raman line at 3054 cm^{-1} and about 9 fold for 50 nm radius array for the Raman line at 1075 cm^{-1}. The experimental values obtained for the same conditions are 11 fold for 60 nm radius array and 10 fold for 50 nm radius array.

4.1.6 Results and Discussion

Benzenethiol has a known packing density and it is a widely used molecule in SERS studies, which makes it an ideal candidate for enhancement factor calculation and comparison with previous reports in the literature. We have used the largest surface packing density reported for benzenethiol in the enhancement factor (EF) calculations ($6.8x10^{14}$ molecules.cm^{-2}) [63, 91, 92]. The homogenity was checked by taking several measurements from different spots on the same sensor area and the repetability of the measurements was found within error bound of ~13%. The measurements were taken right after coating.

The most common EF definition is used for comparison with similar structures that can be written as $EF = (I_{SERS}/N_{SURF})/(I_{RS}/N_{vol})$ [63, 64, 93]. Here, N_{vol} is the number of molecules in the detection volume that contribute to the Raman signal measured from neat, liquid benzenethiol and N_{SURF} is the number of adsorbed molecules that contribute to the measured SERS signal. I_{RS} and I_{SERS} are the Raman and SERS intensities obtained from neat benzenethiol and the nano-lithographed SERS substrates, respectively.

In the Raman experiment, a thin glass container with neat Benzenethiol is used. The probe volume was approximated as a cylinder of height that equals the thickness of neat benzenethiol following the same steps and reasoning as in the works of Chu and Banaee [85, 86] and calculated as 362 fl. The number of probed molecules is determined from $N_{vol} = NA\,\rho hA/M$ where NA is

Avogadro's number, ρ is volume density (1.073 g.cm^{-3}) and M is molar mass (110.18 g.mol^{-1}) of benzenethiol molecules. h is the thickness of the neat benzenethiol sample and A is the spot area. N_{vol} calculated in this way is 2.1× 10^{12} molecules.

In the SERS EF calculations, exposed gold surface area of a single truncated nano-cone is calculated using the SEM measured dimensions for every physically different array. Lateral and top surfaces are taken into account. Lateral surface area of the SiO_2 spacer is excluded from the total calculated area for tandem structures. The number of nanostructures at the spot area is calculated using the period of the truncated nano-cones and spot size of the laser. A perfectly ordered self-assembled monolayer is assumed on the exposed surfaces to calculate maximum possible N_{surf} [63, 91, 92]. Any possible defect at the exposed surfaces due to fabrication imperfections or in the monolayer formation would result in larger EF values. The calculation can be summarized as $N_{surf} = \rho_s S_{gold} A/P^2$ where ρ_s is the surface packing density, S_{gold} is the exposed gold area for a single nano-cone, A is the spot area and P is the period of the array [85]. Note that since the same objective is used in both Raman and SERS experiments, the spot area is actually cancelled out in the EF calculations.

To make a reasonable performance comparison, truncated gold nano-cones that have single resonance wavelength that is matched with the electrical resonance of tandem structures are designed and fabricated. By this way one can observe the enhancement due to the presence of the second resonance with all the other conditions fixed. Baseline corrected SERS data is presented in Figure 4.5a for single resonance and tandem structures along with their optical transmission data. The physical dimensions and schematics of "tandem" and "only gold" structures are provided in Figure 4.1.

As can be seen from Figure 4.5a Benzenethiol has characteristic raman lines at 999 cm^{-1}, 1024 cm^{-1}, 1075 cm^{-1}, 1575 cm^{-1}, and 3055 cm^{-1}. These lines correspond to the C-C-C in-plane ring-breathing mode, the in-plane C-H bending mode, the in-plane ring-breathing mode coupled with the C-S stretching

mode, the C-C stretching mode and C-H stretching mode bonds of the molecule, respectively. The band at 3055 cm^{-1} is characteristically less intense than the others as observed in other studies that occupy gold substrates [91]. Therefore a different intensity scale is used after the axis break at 1750 cm^{-1} to be able to observe the variation at this Raman line especially for the truncated gold nano-cones that have single resonance wavelength.

The optical transmission data presented in Figure 4.5b reveals that the magnetic resonance of the tandem structures with 50 nm bottom radius are tuned for 1000-1600 cm^{-1} and 60 nm bottom radius are tuned for 3055 cm^{-1}. The comparison between the proposed structures is done in terms of EFs to take into account the differences in exposed gold surface areas.

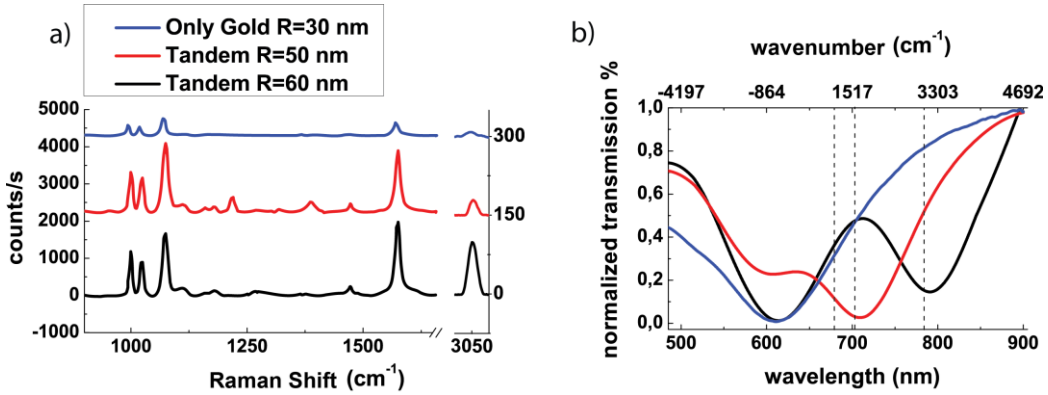

Figure 4.5: (a) Baseline corrected SERS data from "tandem" and "only gold" nanostructures. An axis break is added to the horizontal axis for Raman line at 3055 cm^{-1} since this peak is both distant and not as intense as the other peaks. Spectra are shifted for a better view (b) normalized transmission data for the same "tandem" and "only gold" nanostructures. The spectra are normalized to aid in the comparison of the position of the resonance wavelengths. The same legend applies to both figures. Raman lines at 1075 cm^{-1}, 1575 cm^{-1} and 3055 cm^{-1} are indicated with dotted lines.

The variation in the calculated SERS EFs are presented in Table 4-1 and Table 4-2. In Table 4-1, the EFs calculated for wavenumbers 1075 cm^{-1}, 1575 cm^{-1}, and 3055 cm^{-1} are presented for "tandem" and "only gold" arrays. In Table 4-2, the ratios of the EFs for tandem structures to EFs for single resonance gold truncated cones are listed.

Table 4-1 Calculated SERS Enhancement Factors for "tandem" and "only gold" arrays

	3054 [cm^{-1}]	1575 [cm^{-1}]	1075 [cm^{-1}]
tandem R=60nm	$7.12x10^5$	$2.20\ x10^7$	$2.52\ x10^7$
tandem R=50 nm	$3.23\ x10^5$	$2.55\ x10^7$	$3.86\ x10^7$
only gold R=30nm	$6.38\ x10^4$	$2.51\ x10^6$	$3.80\ x10^6$

Table 4-2 Improvement of "tandem" with respect to "only gold" arrays

	3054 [cm^{-1}]	1575 [cm^{-1}]	1075 [cm^{-1}]
tandem R=60nm	11 x	9x	7x
tandem R=50 nm	5 x	10x	10x

The double resonance "tandem" structures can provide roughly 10 times larger enhancement than single resonance "only gold" structures for the Raman shifted peaks closer to the magnetic resonance frequency for each of the tandem arrays. R=60 nm array exhibits more than an order of magnitude enhancement for 3055 cm^{-1} line whereas R=50 nm array exhibits a similar enhancement for 1075 cm^{-1} and 1575 cm^{-1} lines. The obtained results are in accordance with the simulations and the theory.

4.1.7 Conclusion

In this study, a systematic tuning of the two resonance frequencies of tandem structures was done to maximize SERS EF. The maximum EFs obtained for Au-SiO_2-Au structures for 1075 cm^{-1} is $3.86x10^7$. The double resonance structures were shown to provide 10-fold larger enhancement than their single

resonance counterparts. This value can be further increased in applications such as NIR-SERS and Surface Enhanced Hyper Raman Scattering (SEHRS) where the difference in frequency for excitation and scattering signals is more pronounced.

Gold was selected as the metal due to its chemical stability, biocompatibility and sharp resonance dip at the wavelengths under study. However it is reported in the literature that by using silver as the metal, one can further increase SERS enhancement [85, 94]. So the enhancement values obtained in this study still has room for improvement simply by changing the type of metal.

Another way to increase the enhancement is to selectively etch some portion of the SiO_2 layer and the molecules that reside in this gap will experience a larger electric field than they do on the surface. The hot-spots formed in this way are expected to provide a larger enhancement that may even enable single molecule detection.

4.2 Concentric Ring Structures as Efficient SERS Substrates

This section of the thesis is accepted by IEEE Journal of Selected Topics in Quantum Electronics (JSTQE) under the heading "*Concentric Ring Structures as Efficient SERS Substrates*" by Neval A. Cinel, Semih Çakmakyapan, Gülay Ertaş, Ekmel Özbay, to be published in "Nanophotonics special issue", May/June 2013.

4.2.1 Introduction

In this study, SERS active substrates are fabricated with E-beam lithography to assemble reproducible arrays that can tailor the SERS efficiency and enable parameter optimization. Two different designs are prepared for comparison. The first set constitute, circular concentric rings etched from a planar gold film. In the second set, the etched portions are filled with a dielectric

spacer and a second layer of golden rings are deposited only at the top of the dielectric spacer forming a coupled ring structure. The performance of "coupled ring" samples are compared to those with "etched ring" samples and "plain gold" film via SERS experiments and simulations. It is also shown that the design can be tuned physically for better SERS performance.

Similar designs such as concentric arcs [95] and concentric rings [96] milled into metallic films are also available in the literature to be used as SERS substrates. These designs mainly depend on focusing the propagating surface plasmons at the center of the rings for SERS enhancement. However, our motivation in this study is to show that the proposed dual layer concentric ring structure can provide increased electric field intensity due to the coupling of plasmons localized between the rings and the center disk.

4.2.2 Fabrication of Concentric Ring Structures

The fabrication of the concentric ring samples start with the spin coating of the sapphire substrate with Poly(methylmethacrylate) (PMMA 950 A-2) resist at 2500 rpm for 40 seconds. It is baked for 90 seconds at 180ºC and the Hydrogen silsesquioxane (HSQ) negative tone electron-beam resist is spin coated at 2000 rpm for 40 seconds. The substrate is then baked again for 90 seconds at 150ºC and aqua-save (polymer) coating is done to reduce the charging effects during e-beam exposure. After lithography is performed with the "RAITH E-Line" system, the substrate is developed in Tetramethyl Ammonium Hydroxide (TMAH) for 75 seconds. TMAH developer removes the unexposed parts of HSQ resist, leaving behind the ring patterns residing on the preserved PMMA resist layer. To remove the PMMA under the HSQ mask, O_2 plasma etch is done by the "Sentech SI 500 ICP-RIE Dry Etching System" at a 50 W RF and 100 W ICP power for a duration of 30 seconds. Finally, 5 nm Ti adhesion layer and 40 nm Au is evaporated on the patterned sample by "Leybold Univex 350 Coating System". This ends the fabrication of the "coupled ring" structure as shown in Figure 4.6b. For the "etched ring" sample shown in Figure 4.6c, a final lift off step in acetone is necessary to resolve the remaining PMMA

under the upper rings. The fabrication steps are visualized in Figure 4.6a for a 5-ring "coupled" structure. The SEM image of the resultant structure is shown in Figure 4.6d.

Physically different structures that have varying dimensions are fabricated to optimize the SERS signal intensity. The number of rings for different samples are chosen as 18 considering that the increased number of rings is expected to increase the resultant E-field intensity [97]. The inner disk diameter changes from 0.965 μm to 1.750 μm. The period of slits vary between 500-860 nm.

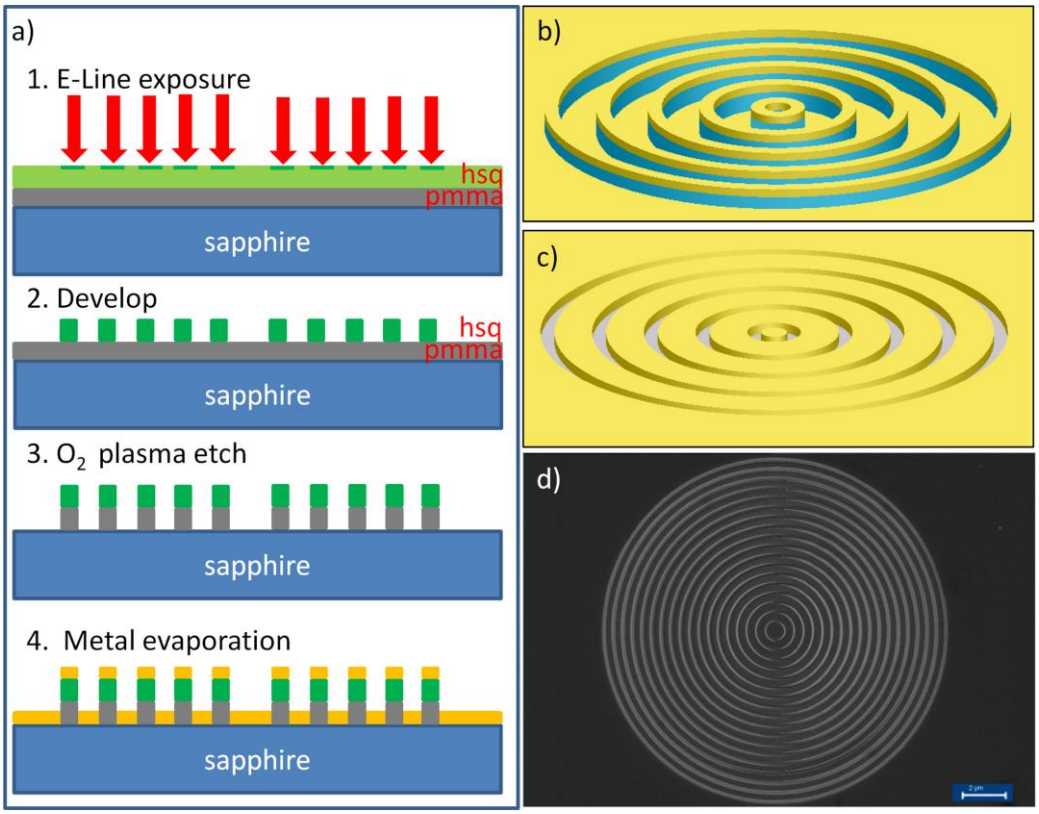

Figure 4.6: (a) Illustration of fabrication steps for a 5-ring "coupled" structure (b) conceptual image of "coupled" concentric rings (c) conceptual image of "etched" concentric rings (d) SEM image of the coupled structure. Inner ring diameter 965 nm, period 500 nm. The scale bar corresponds to 2 μm.

4.2.3 Fluorescence Imaging

There are several methods to visualize the plasmon fields accompanied by nano structures. The most convenient method for surface plasmon (SP)

imaging is to use near-field optical microscopy [98]. A more practical way is to distribute fluorescent molecules homogeneously close to the metal surface and use optical microscopy [99]. The fluorescent molecules should be positioned at a distance from the metallic surface preferably by a few nanometers thick dielectric layer since fluorescence can quench in direct contact with the metal.

Momentum matching between light and SPs is maintained by the corrugations on the gold surface. A high flux red LED is used for excitation purposes. A Leica optical microscope and its integrated CCD is used to observe and image the surface. The 100X objective with numerical aperture 0.9 is used. The thin dielectric spacer is maintained by the Benzenethiol monolayer coated for SERS measurements. No other means of dielectric deposition was necessary and no fluorescence quenching effect was observed. A monolayer of Rhodamine 6G molecules were deposited on the spacer layer by incubating the samples for 1 hour and post-cleaning several times with deionized water (DI) to remove any residue after incubation. The images obtained in this way represent the SPs qualitatively rather than in a quantitative way [99]. The presented data is in accordance with the near field energy density distribution measurements done with NSOM for a plasmonic lens structure made of multiple concentric metallic rings similar to our proposed design [98].

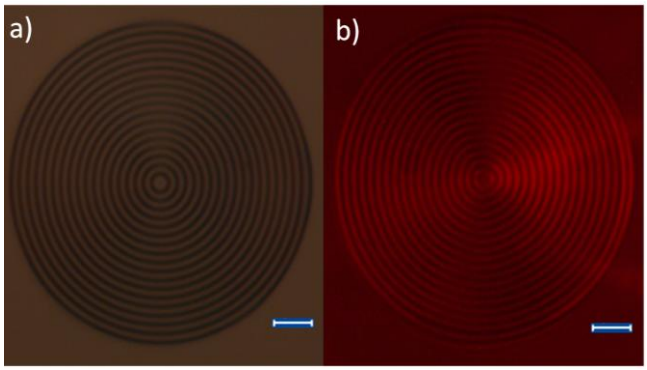

Figure 4.7: (a) Optical microscope image under white light illumination (b) imaging of surface under LED excitation. The scale bar corresponds to 2 µm for both figures.

4.2.4 FDTD Simulations

A commercial software package called “Lumerical” relying on finite difference time domain (FDTD) technique is used in the simulations. All the physical boundary conditions are chosen as perfectly matched layer (PML) to avoid undesired reflections from boundaries. A maximum mesh size of 5 nm is used in the simulations to save computation time while preserving accuracy. 2-ring counterparts of the proposed structures are used for comparison to save computational sources. The physical dimensions of the disk and the rings are the same as the fabricated structures except the number of rings. The 5 nm Ti adhesion layer is excluded and a 45 nm gold layer is assumed in the simulations considering the maximum mesh size would not resolve the thin Ti layer. The material data for sapphire and gold are taken from the works of Palik [70] and Johnson and Christy [90], respectively. The structures are illuminated with a single wavelength plane wave source at 632.8 nm that matches the laser excitation wavelength. 2D cross-sectional monitors are used to visualize the E-field distributions. Coupled structures that provide the best and worst signal intensity (corresponding to the resonant and non-resonant conditions) and etched ring structures are compared.

In accordance with the SERS experiments, the coupled structures end up with a higher E-field intensity distribution and hence higher SER intensity as can be seen in Figure 4.8. In the resonant coupled structure, the upper rings are coupled to the bottom rings which results in the increase of “hot spots” responsible for the enhancement. This is degraded for the non-resonant structure and minimized for the etched-ring structure.

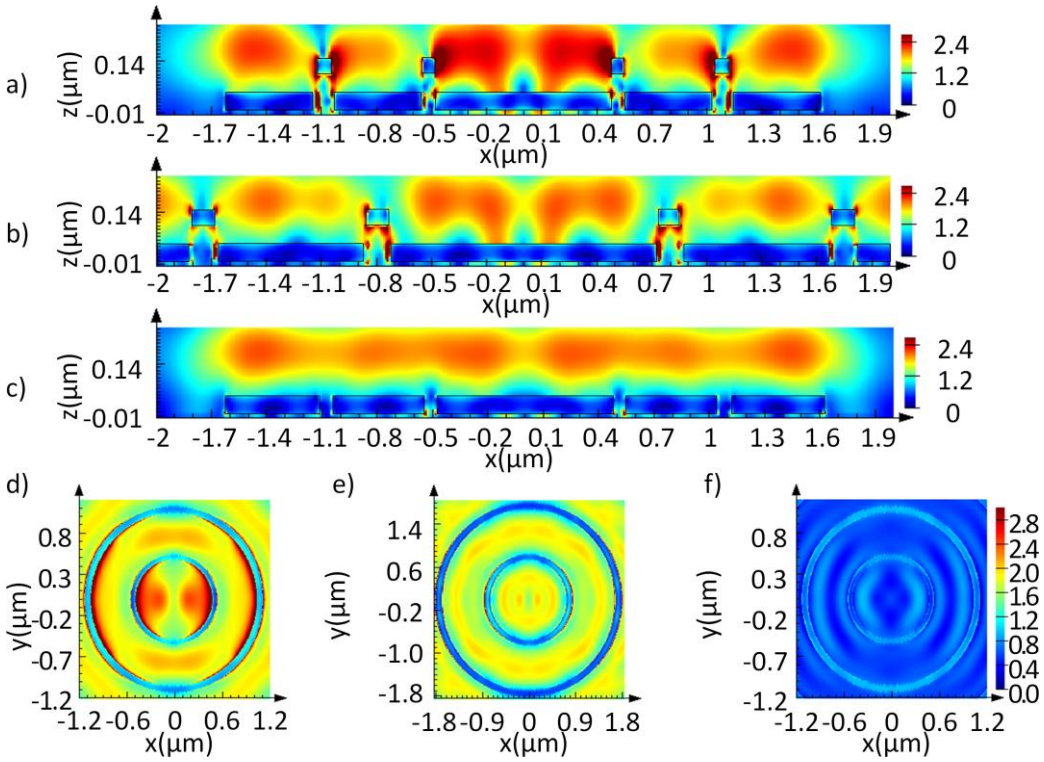

Figure 4.8: Cross sectional E-field distributions ($|E|^2$) of the coupled resonant (a, d), coupled non-resonant (b, e) and etched ring (c, f) structures, respectively. Same color scale is used for d, e and f.

The experimentally obtained enhancement from the resonant coupled structures with respect to the etched structures is also validated by simulations. The SERS intensity is considered to be proportional to $|E|^4$ at the laser excitation frequency for this calculation. The E-field distributions obtained through simulations are integrated over the gold surfaces for both designs using 4 µm spot size. The resultant ratio gives Total $|E|^4_{coupled}$/ Total $|E|^4_{etched}$ ~12 which is close to the experimentally derived 8 times larger signal intensity. The difference between simulations and measurements can attributed to imperfections in fabrication and surface preparation or spot size determination.

4.2.5 SERS Experiments and Results

The SERS data is collected under excitation with a He-Ne laser at 632.8 nm with the Horiba LABRAM system. 100X objective with a 0.9 numerical aperture is used throughout the measurements. A slit size of 200 µm and a hole size of 1100 µm ended up with the best resolution. The samples to be measured

are incubated in 100 mM benzenethiol in an ethanol solution for 2 hours and then thoroughly rinsed with ethanol to ensure a self assembled monolayer formation on the surface and to remove residues. The measurements are taken right after coating. The missing S-H bonds (at 2550-2600 cm^{-1}, not shown in the graphs) in the SER spectrum verify that Au-S bonds are formed and indicates the formation of a monolayer [100]. Benzenethiol was purchased from Sigma-Aldrich and used as is in the Raman experiments.

Same integration and exposure times are used for all the samples except for the "plain gold" sample. Although 4 times larger integration time is used for the "plain gold" sample, no distinguishable signal is observed. Considering the maximum intensity obtained from "coupled ring" structures and the minimum detectable intensity throughout the experiment it is derived that patterned structures have at least 630 times larger SER intensity when compared with plain gold film. The data is presented in stack form in Figure 4.9 for easy visual comparison.

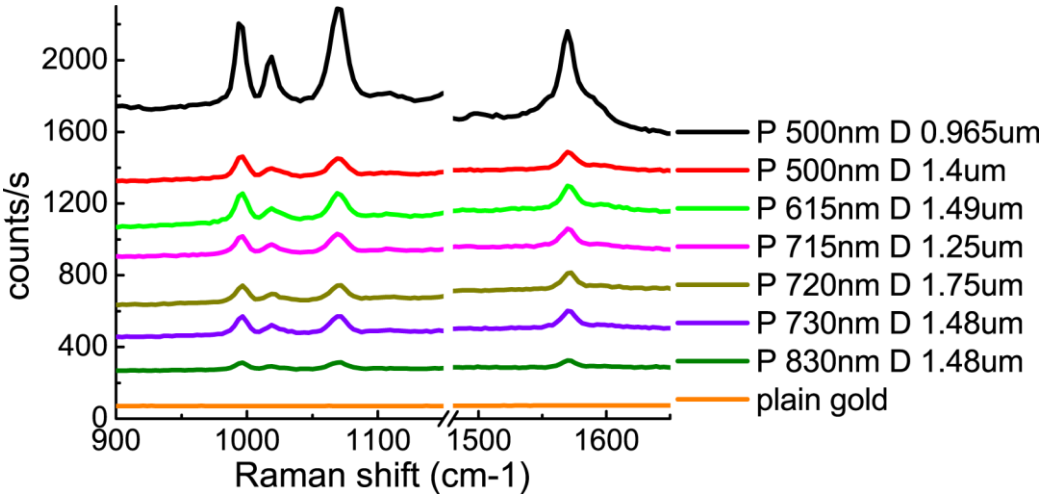

Figure 4.9: SER spectra of Benzenethiol from the "coupled ring" structures and plain gold film. No background correction is done. Spectra are shifted for a better view. A horizontal axis break is applied to save space. In the legend, the letter "P" denotes period and the letter "D" denotes diameter.

For all the fabricated samples, the number of rings is the same and the slit widths are close to each other. Therefore, the change in signal intensity may be due to the inner ring diameter and the period. The acquired SER signal from

different samples shown in Figure 4.9 indicates that, the sample with the smallest inner ring diameter has the largest signal intensity. One reason for this situation may be the increase in the number of rings (and, therefore, the number of hot-spots) that is included within the laser spot area, as the inner radius decreases. The increased E-field intensity is considered to be mainly due to the interaction (coupling) of the upper rings residing on dielectric and lower rings residing on sapphire. This coupling can also be visualized from the simulation results presented in Figure 4.8. The period does not seem to create a major impact on the resultant signal for this design, when considered in combination with the other design parameters.

The effect of coupling between the upper and lower rings is also studied by comparing the “coupled” and “etched” ring structures. The coupled structures shown in Figure 4.6b have upper and lower rings separated by a dielectric spacer layer whereas the etched ring structures only have the lower rings as shown in Figure 4.6c. The “etched ring” structures are similar to the plasmonic lens designs that exist in the literature [97]. In a plasmonic lens structure, the period has to be chosen so as to match the surface plasmon wavelength to maximize the focusing and, therefore, the E-field intensity that dominates the resultant SERS signal intensity [101, 102]. Accordingly, the period of the “etched ring” structure is chosen close to the surface plasmon wavelength (calculated as 605 nm corresponding to the incident wavelength of 632.8 nm) in order to maximize the focusing. The SERS experiments show that the “coupled ring” structure that has similar physical dimensions with the “etched ring" structure gives 8 times better signal intensity than such an optimally designed plasmonic lens structure as depicted in Figure 4.10.

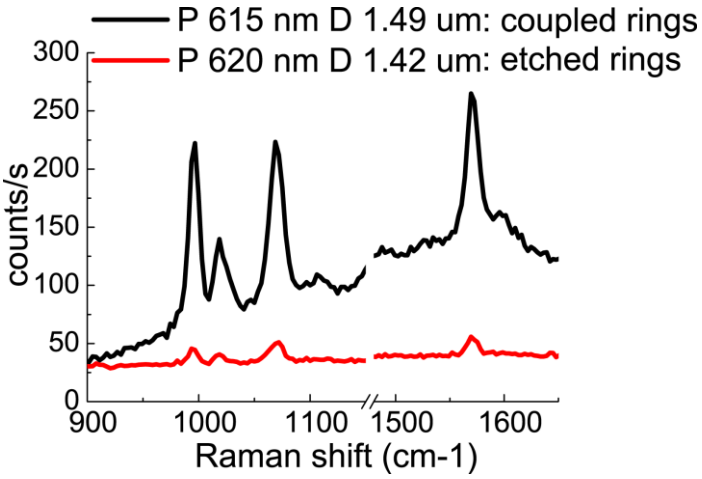

Figure 4.10: SER spectrum of Benzenethiol from the "coupled" rings and the "etched" rings. No background correction is done. A horizontal axis break is applied to save space. In the legend, the letter "P" denotes period and the letter "D" denotes diameter.

As also mentioned in Section 4.1.6 , an objective measure to compare the performance of different designs existing in the literature is the enhancement factor (EF) calculation. The same EF definition as in Section 4.1.6 is used and similar steps are followed in the Raman experiment. The exposed gold surface area of the structures is calculated by taking into account the lateral and top surfaces of the rings and the disk. The strongest band in the spectra at 1075 cm^{-1} is employed for the EF calculation.

The EF calculated as described above is $1.67x10^7$ for the coupled-concentric ring structures. On the other hand, the conventional SERS EF is on the order of 10^6 [103]. Therefore, we can conclude that, the coupled-concentric ring structure can be a strong candidate for increasing efficiency in SERS experiments.

4.2.6 Conclusion

We present here our preliminary results in designing plasmonic nano-patterned structures that can work as highly efficient SERS substrates. We relate the obtained results with theory and support with simulations. The proposed design gives 630 times larger signal intensity than "plain gold" film and 8 times larger than an optimally designed "etched-ring" plasmonic lens structure.

Coupling between the upper and lower rings is visualized through simulations and is believed to increase the number of "hot spots" responsible for the enhancement. The calculated EF of $1.67x10^7$ can still be improved through tuning the physical dimensions of the structures.

Future study includes the investigation of the optical responses through reflection-transmission measurements and tuning the resonance of the structures for a better match with the laser excitation frequency to obtain a better SER signal. Under such resonant excitation the enhancements obtained thus far are expected to increase significantly [104]. The relationship between the signal intensity and the physical sizes and parameters such as slit width, number of rings, thickness and material of the separation layer and period should also be further studied.

Chapter 5

UV Photodetectors Utilizing Plasmonics

This chapter mainly deals with utilization of plasmonics for UV-MSM photodetectors. In the first part, an LSPR enhanced MSM UV photodetector on semi-insulating GaN is presented. The design employs plasmonic Al nanoparticles fabricated in between the metallic electrodes to increase the absorption in GaN. In the second part, a nano-antenna coupled UV subwavelength photodetector on GaN is introduced. The design includes a subwavelength aperture surrounded by a nano-structured metal grating and compared to a conventional MSM photodetector employing only a subwavelength aperture. In both studies, device characterizations were done by optical transmission, responsivity and I-V measurements.

5.1 LSPR enhanced MSM UV photodetectors

This chapter is published under the title “LSPR enhanced MSM UV photodetectors” by Serkan Bütün, Neval Ayşegül Cinel and Ekmel Özbay, at “Nanotechnology”, Vol. 23, Issue 44, pp. 44010-44010-5, November, 2012.

5.1.1 Introduction

In this part of the thesis, we have fabricated MSM photodetectors working in the UV region, on semi-insulating GaN grown at MOCVD (Aixtron AG AIX 200/4 RF-S) facilities of Nanotechnology Research Center, Bilkent University. The performance of the photodetectors is shown to increase by 50% with the insertion of plasmonic nanoparticles whose resonance lies at the UV region, in between the Schottky contacts of the photodetector. The conceptual drawing of the MSM photodetector is shown in Figure 5.1.

The material choice for nanoparticles was dominated by the need for resonance at UV wavelengths. The most suitable metal for supporting plasmon resonance at this spectral range is Aluminium. The insertion of the nanoparticles created a comparable difference on the quantum efficiency of the device.

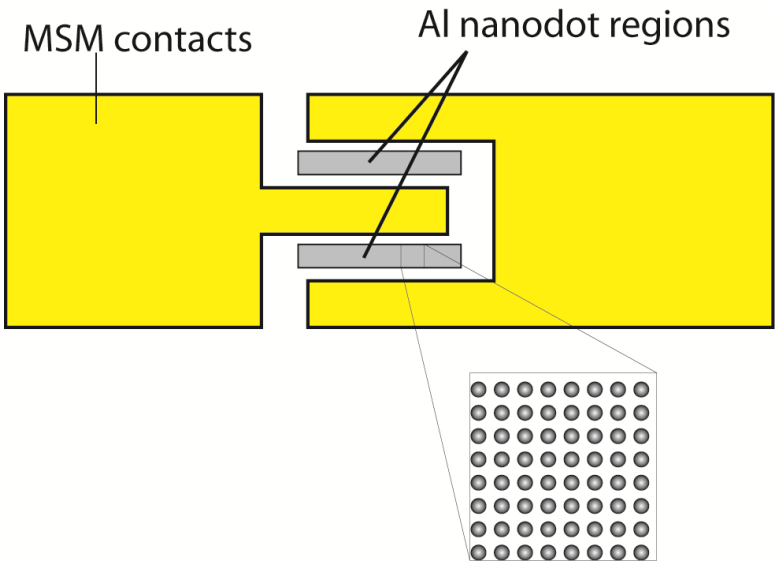

Figure 5.1: Conceptual drawing of LSPR enhanced MSM UV photodetectors (top view). The Aluminium nanoparticles are inserted in between the Schottky contacts of the detector.

5.1.2 Growth and Fabrication

Semi-insulating (SI) GaN for MSM photodetectors are grown with low-pressure metal organic chemical vapor deposition (MOCVD) on c-face (0001) sapphire substrates annealed at 1100 °C for 10 min to remove surface contamination. After anneal, a 15 nm thick AlN nucleation layer was deposited at 840 °C, followed by AlN buffer layer growth at 1150 °C reactor temperature. Finally, GaN is grown at 200 mbars reactor pressure, 1070 °C growth temperature, growth rate about 2 μm/h with H_2 carrier gas and trimethylgallium (TMGa), trimethylaluminum (TMAl), ammonia (NH3) used as the Ga, Al, and N precursors, respectively [105].

Fabrication of the Schottky contacts was done by image reversal optical lithography since the contact pads are large to write with EBL. Clean substrates are spin coated with TI35E photoresist and pre-baked at 110°C for 120 s. Then

they are exposed to UV over the mask that is aligned and positioned with Karl Suzz MA6-Mask aligner and the contact pad patterns are transferred to the photoresist. After AZ400K developer is used to remove exposed parts of the photoresist, the sample is ready for the metallization. The Ni/Au contact metallization is done in e-beam evaporator with metal thicknesses 10/150nm, respectively. Nickel is selected for its good Schottky performance on GaN and gold is selected to protect against oxidation while increasing the conductivity. The distance between interdigitated fingers is 20 μm.

Different diameter nano-dot arrays with varying periods were fabricated by EBL in order to tune the plasmonic resonance to the desired wavelength. Similar fabrication steps are used as described in Chapter 3. Same dimension arrays are fabricated on both GaN and sapphire substrates, the latter to be used for optical transmission measurements. The radii and the period of the resultant arrays vary between 10 to 30 nm and 100 to 200 nm, respectively. The total write-field is 50 × 50 μm^2. The same transmission set-up is used for extinction measurements as in Chapter 3. Size and the period of the particles are verified with scanning electron microscopy (SEM). The optimal size is found to be 18 nm in radius and 100 nm in period considering the optimum resonance wavelength. The SEM image of the fabricated size-optimized aluminum nano-dots is shown in Figure 5.2 along with the size distribution graphics emphasizing the uniformity of the resultant array.

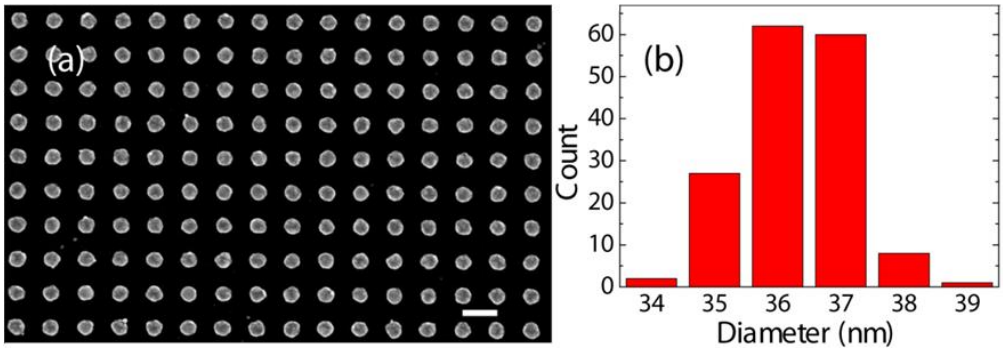

Figure 5.2: (a) SEM image of the EBL fabricated Al nanoparticles. Scale bar is 100 nm. (b) Size distribution of the particles in (a).

5.1.3 Measurements and Simulations

The transmission characteristics of different sized Al nano-dot arrays are studied by spectral transmission measurements and verified by FDTD simulations using Lumerical software (Figure 5.3). Both results are in accordance with each other and they indicate that as the nano-dots get larger the extinction peak shifts toward longer wavelengths with an increased resonance intensity, similar to the case observed in LSPR biosensor study described in sections 3.1.5 and 3.1.7. Another important point to note is that the transmission measurements are done for nano-dots fabricated on sapphire that is transparent at the wavelengths under study. The actual devices on GaN result in a red-shifted response since GaN has a higher refractive index than sapphire which is in accordance with the theory as described in Section 2.1.1 and experimental observations that imply enhancement around 339 nm which is red-shifted with respect to the design on sapphire.

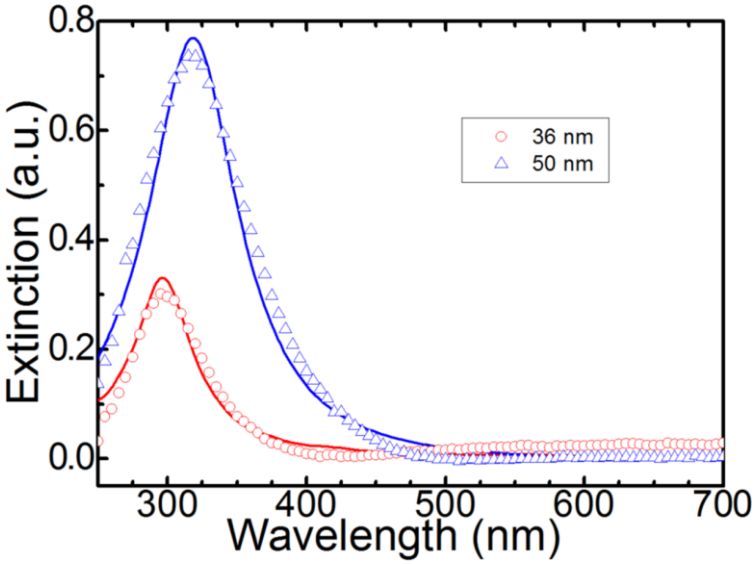

Figure 5.3: The extinction spectra of the Al nano-particles on sapphire. Legend indicates the diameter of the particles. Period is 100nm. Dots represent the measurements, lines represent the simulations.

Another simulation is done to visualize the electric field distributions of the aluminium nanoparticles (Figure 5.4). Results show that at resonant wavelengths, there is a strong confinement in the dielectric compared to an off-

resonant case. This provides further evidence that the plasmonic nanoparticles enhance absorption in the semiconductor at illumination wavelengths close to their resonance peak.

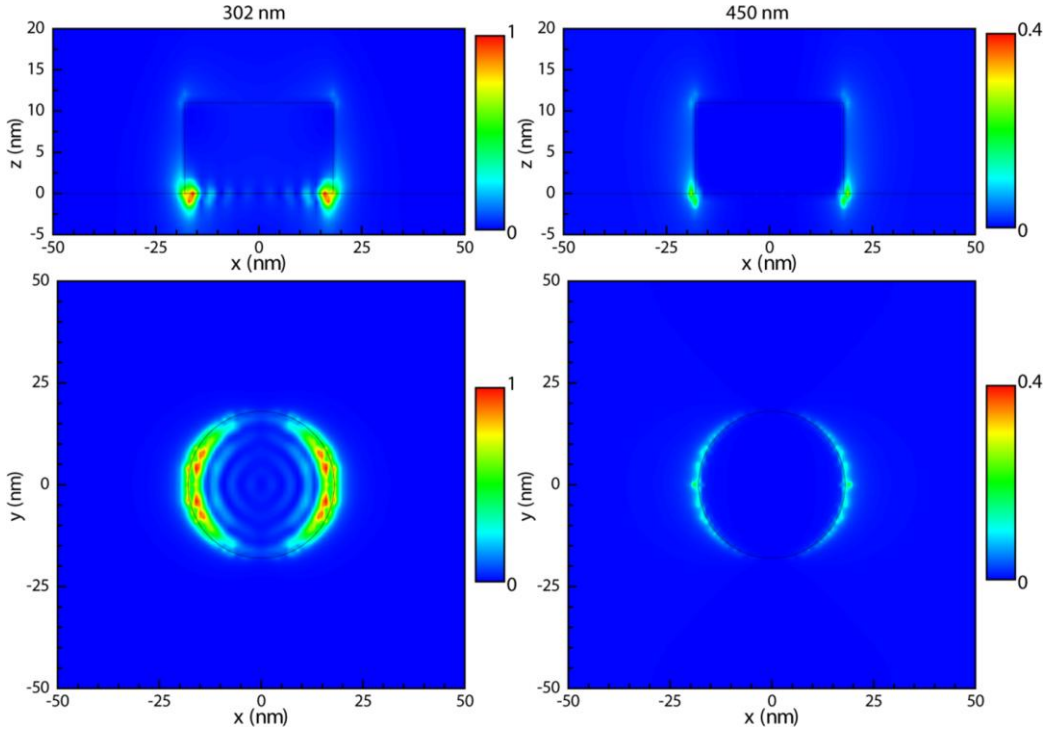

Figure 5.4: Crossectional electric field distributions of the aluminium nanoparticles on sapphire substrate calculated via FDTD simulations. On the left, normalized (to the maximum value) E-field intensity distributions at a resonant wavelength of 302 nm are shown. Distributions at an off resonant wavelength of 450 nm are presented on the right for comparison. z direction is normal to the surface and the sapphire/air interface lies within the z=0 plane.

Photodetector characterization requires the estimation of spectral responsivity. For this aim, we used a custom made spectral responsivity set-up including a xenon arc lamp (Spectral Products ASB-XE-175), a monochromator (Spectral Products DK240), an optical chopper, a calibrated Si photodetector (Newport 818-UV-L) and a lock-in amplifier (Stanford Research Systems SR830) as shown in Figure 5.5. The output of the xenon lamp is fed to the monochromator to select the illumination wavelength of incident light. The monochromated light is then pulsed with a rotating disk chopper and sent through a fiber probe to illuminate the photodetector from the top. Photocurrent

was measured by lock-in amplifier that is synced with the chopper to reduce noise from external light sources as a function of wavelength.

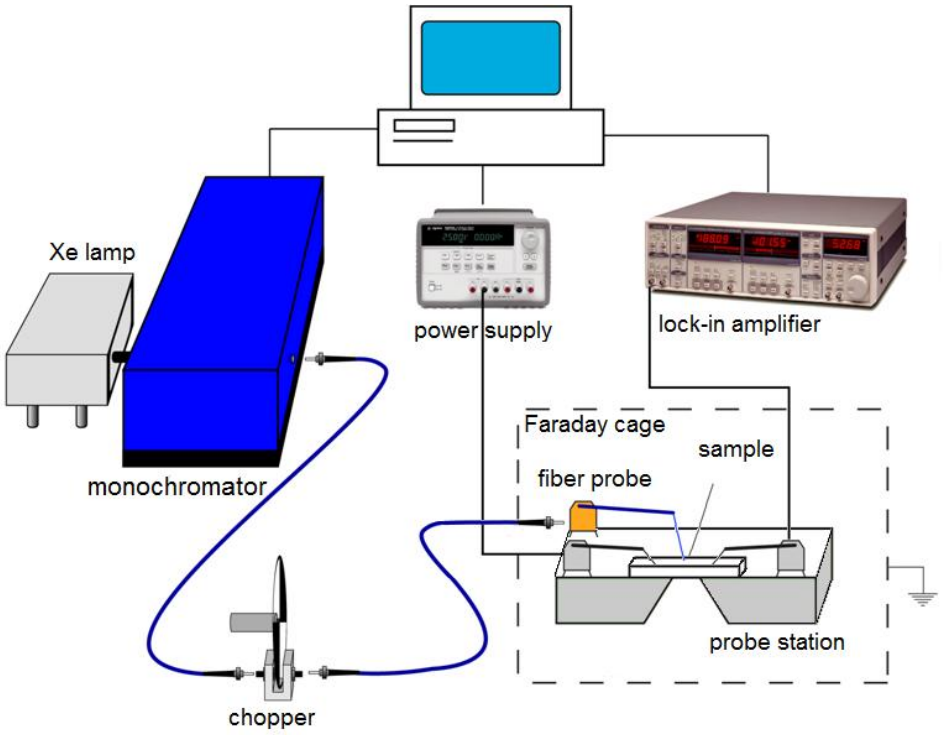

Figure 5.5: Schematic drawing of photoconductivity setup.

A reference measurement is necessary to determine the incident optical power as a function of wavelength in responsivity calculations. The NIST-traceable, calibrated Si photodetector with known spectral responsivity is used for this purpose and therefore the photocurrent normalization. Then a photocurrent measurement is performed with the MSM photodetector. The measured detector current and the reference power measurements in combination determine the responsivity as described in Section 2.2.

5.1.4 Results and conclusion

The quantum efficiency is derived from the responsivity measurements for both the control sample and the GaN photodetector with Al nano-dots as shown in Figure 5.6(a) using the relation described in Section 2.2. This figure together with the enhancement of quantum efficiency shown in Figure 5.6(b)

implies that there is nearly 1.5 fold enhancement in the quantum efficiency in the presence of plasmonic nanoparticles when compared with the control sample. This can be explained with strongly localized electromagnetic field at the metal-dielectric boundary at the plasmonic resonance wavelength of the aluminium nanoparticles around 340nm where the enhancement is observed. The data after 360nm is not presented in Figure 5.6(b) since GaN band edge absorption occurs around here. GaN is already transparent at longer wavelengths which provides its "visible blindness" and therefore this part has no physical meaning.

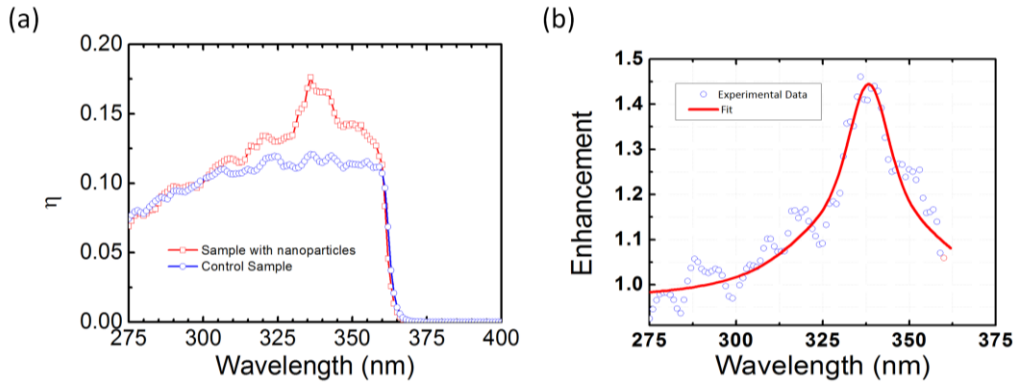

Figure 5.6: (a) Comparison of quantum efficiencies in the presence of plasmonic nanoparticles and the control sample (b) Enhancement of the quantum efficiency in the presence of plasmonic nanoparticles

To conclude, in this study we studied the utilization of LSPR in UV-MSM photodetectors. The plasmonic resonance of Aluminium nanoparticles at UV wavelengths are shown to increase absorption and photocurrent collection at the GaN active layer of the photodetector. The spectral tuning of the nanoparticles was done through optical transmission measurements along with SEM based dimension estimation. The enhancement in quantum efficiency is shown through responsivity measurements. The calculated 1.5 fold enhancement in the presence of nanoparticles proves the claim.

5.2 Nano-antenna coupled UV subwavelength photodetectors based on GaN

This chapter is published as "Nano-antenna coupled UV subwavelength photodetectors based on GaN" by Serkan Bütün, Neval Ayşegül Cinel and Ekmel Özbay, Optics Express, vol. 20, issue3, pp. 2649-2656, January, 2012.

5.2.1 Introduction

In this part of the thesis, we designed another MSM photodetector working in the UV region, on semi-insulating GaN grown similarly as described in Section 5.1. A nano-antenna composed of Al gratings was integrated to the detector for photocurrent enhancement. The resultant design is composed of a subwavelength aperture surrounded by a nano-structured metal grating and compared to a conventional MSM photodetector employing only a subwavelength aperture. The conceptual drawing of the nano-antenna coupled UV photodetector is shown in Figure 5.7.

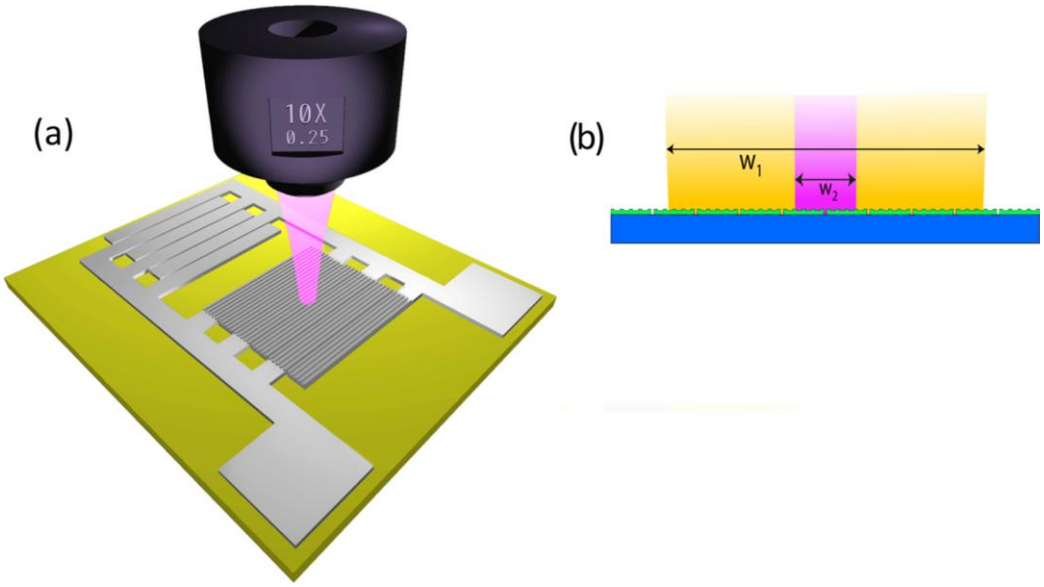

Figure 5.7: Conceptual drawing of nano antenna coupled MSM photodetector is given in (a). (b) A sketch illustrating the width of the illumination beam in spectral (w_1) and laser (w_2) measurements.

We followed the same reasoning in the material choice for the designed nano-antenna as in Section 5.1. The integration of the size optimized Al grating nano-antenna created more than seven fold enhancement in photocurrent. Size optimization was done through reflection measurements. FDTD simulations were done to reveal the mechanisms that play a role in the photocurrent enhancement.

Diffraction and transmission of light through a subwavelength slit has long been studied by the pioneers of optics. The discovery of extraordinary transmission through subwavelength hole arrays perforated on the surface of a metal film opened a new path to these studies [16]. The phenomena was attributed to the coupling of light with plasmons. Several researchers studied one dimensional counterparts of this perforated metallic films, namely one dimensional slit arrays [106-108]. These studies showed that the one dimensional slit arrays can be highly transmissive at wavelengths larger than the period of the grating as a result of coupled SPPs on the surface of gratings and cavity modes inside slits [106]. Finally, transmission of light through a slit surrounded by corrugations on a metal film was investigated both theoretically and experimentally [109, 110]. This same phenomenon can also be used in absorption enhancement in an active dielectric material. In this case, the gratings act as antennas to collect and concentrate the signal into a reduced detector volume [111]. Such a design can also help to achieve a higher signal-to-noise ratio (S/N) and faster response. There are several reports implementing or simulating plasmonics based MSM photodetectors employing subwavelength slits and different geometry gratings for various active materials and working frequencies [112-116]. Here, light absorption enhancement relies on capturing and delivering more optical power to the absorbing active regions of the device. There is still debate on the actual mechanisms that influence the enhanced transmisssion/absorption which is out of the scope of this work, but both evanescent waves and SPP are considered to be effective [117].

5.2.2 Fabrication

Photodetector fabrication was done by EBL (Raith E-line system) in two steps. Polymethyl methacrylate (PMMA) 950A was used as the e-beam resist and (1:3) methyl-isobutyl-ketone: isopropanol (MIBK:ISO) solution was used as developer. Firstly, the interdigitated MSM contacts and access pads were written. For the 320 nm UV excitation, the propagation length is calculated as 4.2 μm using Equation (2.3). Accordingly, MSM contact width was chosen as 3 μm in order to be below this value. Ni/Al metal coating of the contacts was done by e-beam evaporation (Leybold Univex 350 Coating System), with thicknesses 10 nm/100 nm, respectively. Secondly, the gratings were written as a 150x150 μm^2 region on top of MSM contacts and 35 nm Al is evaporated as the grating metal. The size optimized sample has a grating period of 314 nm and grating width of approximately 105 nm. The same sample has two separate MSM contact regions with and without gratings, for comparison. See Figure 5.7 (a).

A similar fabrication was done on sapphire substrates for size optimization purposes and these samples were used in reflection measurements. Various grating periods were written on top of MSM contacts with the slit spacings, metal type and thicknesses remaining unchanged. Samples composed of MSM contacts and access pads but without gratings were prepared for the reference measurements, too.

5.2.3 Measurements and Simulations

Reflection measurements were done by Sentec 850 model ellipsometer that has a micro-spot adaptor. We have taken measurements from samples with and without gratings. Both the reference and the grating samples had same sized slits**.** The reflection data of the gratings were normalized by the data of the reference sample. The angle of measurement was 70°. Gratings were aligned perpendicular to the plane of incidence. The measurements are presented in Figure 5.8.

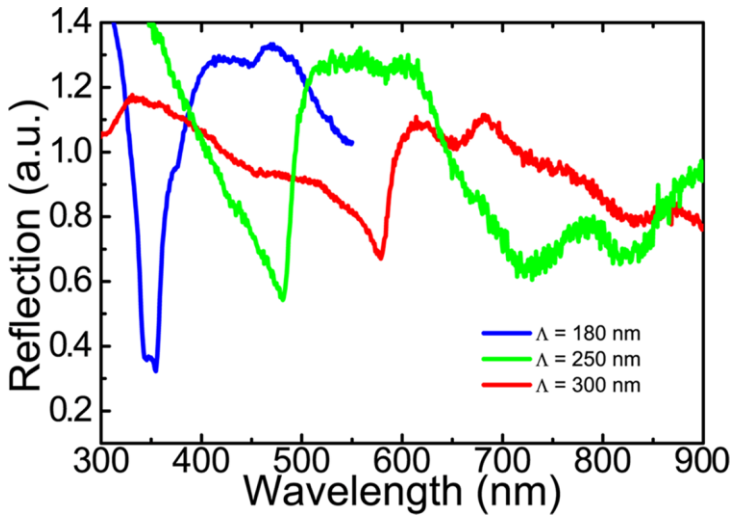

Figure 5.8: Spectral reflectance measurements of the Al gratings with different periods.

We have used a responsivity set up similar to that described in Section 5.1 for the characterization of the device. The same set up was used except the output of the Xenon light source was polarized after being monochromated and coupled to a 10X UV objective with a numerical aperture of 0.25 instead of a fiber probe after being mechanically chopped. The rest of the measurement steps were the same. The measurement was repeated with a linearly polarized 325 nm wavelength He-Cd laser source, to make a comparison. The spot sizes are different for these two measurements as indicated in Figure 5.7(b). In spectral measurements we had 20 μm spot size whereas in laser measurements we had a 3μm spot size. He-Cd laser source has 3 orders of magnitude higher optical power than the spectral setup.

The measured spectral photocurrent data for both samples are compared in Figure 5.9(a) and the enhancement calculated from this measurement is shown in Figure 5.9(b). The peak photocurrent value for illumination over the grating site is 24.5 pA, whereas it is 3.4 pA for illumination over the reference site at zero volt bias, for 322 nm at which the peak enhancement is achieved. These values correspond to the responsivity values of 1.7 mA/W and 0.2 mA/W, for the grating and the reference samples respectively. There is an enhancement factor of about 8 at 322 nm in terms of responsivity as shown in Figure 5.9(b).

In the laser measurements, the photocurrent in TM mode was 60 nA at the grating site, where as it was 9 nA at the reference site. The photocurrent in TE mode was 9 nA and 8 nA for grating site and the reference site, respectively. We can conclude that spectral and laser measurements are in good agreement.

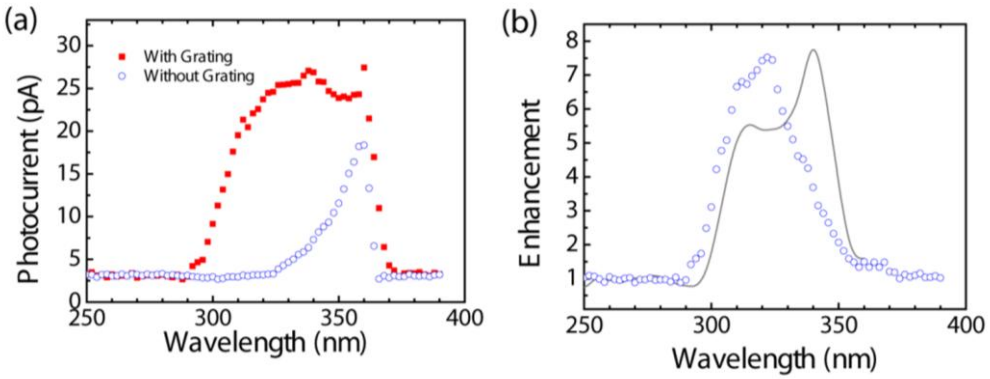

Figure 5.9: Photocurrent measurements of the samples with and without gratings is shown in (a) The corresponding spectral enhancement is shown in (b) Measurements are shown by the dots, the FDTD simulations are shown by the solid line.

The current-voltage (IV) characteristics are also measured (Figure 5.10(c)) in order to prove that MSM contacts are not shorted. The results indicated that, even if MSM contacts are as close as 150 nm (see Figure 5.10(a) and (b)), the leakage current remained below 1 pA up to 7 V bias; so they are well isolated. The device break down voltage is measured around 15 V that corresponds to a field strength of over 1.0×10^{6} V/cm. Withstanding such a high field strength indicates that our GaN material has superior epitaxial quality.

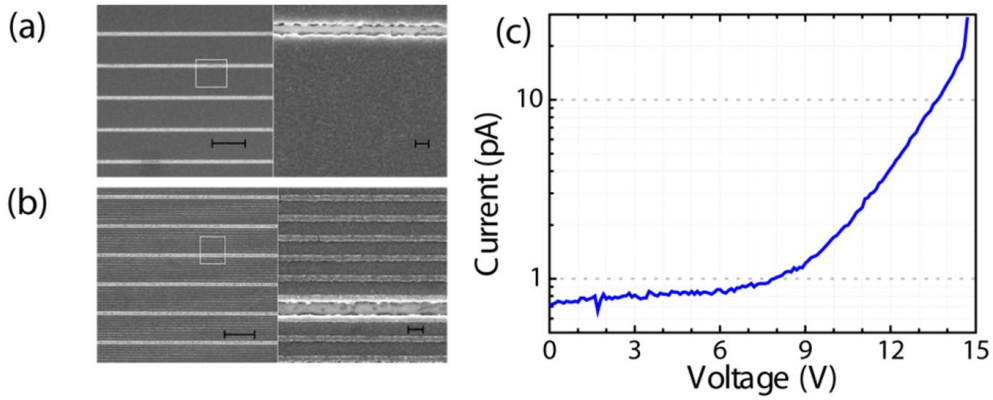

Figure 5.10: Scanning electron microscopy images of MSM contacts (a) without the grating and (b) with the grating fabricated on top. The longer and the shorter scale bars correspond to 3 µm and 200 nm, respectively.(c) dark current-voltage characteristics of the photodetector.

2D simulations were also performed to verify the optical measurements. A commercial software by Lumerical Inc. that relies on FDTD algorithm was used for the simulations. The material data of Al and GaN were taken from Palik [70] and Brunner *et.al.* [118] respectively. Mesh sizes were set to provide sufficient numerical accuracy while keeping the simulation time and memory at a reasonable level. The boundary conditions were all set as perfectly matched layer (PML) in order to eliminate undesired reflections from boundaries.

The total absorbed light intensity was calculated by the integration of the E-field intensity for both structures with and without the metal gratings under TM illumination. The enhancement in absorption is the ratio of the calculated value for the grating sample to the reference sample. The same simulation is repeated for aluminium, gold, silver and perfect electrical conductor (PEC) gratings. Figure 5.11(a) presents the calculated enhancement results for the same device dimensions but with different grating metals in a comparative manner. Figure 5.11(c) and (d) compares the total amount of absorbed light at a resonant (340 nm) and an off-resonant (280 nm) wavelength, respectively.

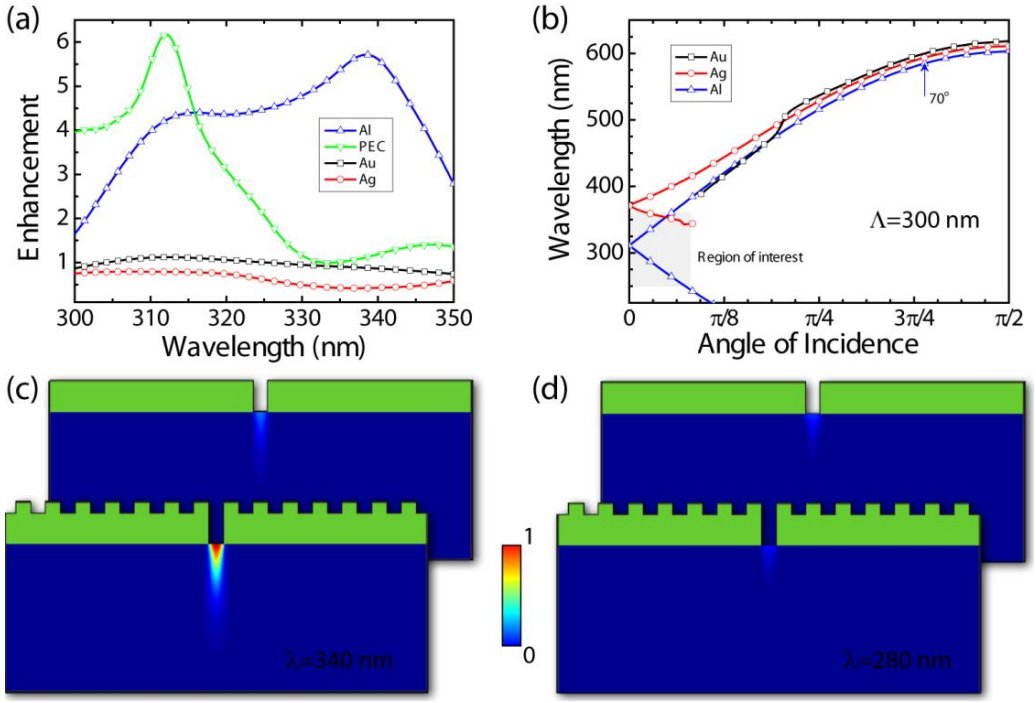

Figure 5.11: FDTD simulations of the nano-antenna coupled MSM photodetectors. (a) The spectral absorption enhancement results for different grating metals. The common device dimensions for all types of metals: Slit width: 100 nm, base height: 75 nm and groove height: 35 nm. (b) Calculated SPP dispersion relation of the grating/air interface for different metals with a grating period of 300 nm. The region of interest indicates the intersection of the wavelengths that GaN has high absorption and the angles in the illumination cone of the objective lens. (c) and (d) comparison of the overall normalized E-field intensity under the slits with and without the gratings at a resonant and an off-resonant excitation. (The color bar applies to all)

5.2.4 Results and discussion

The dispersion relation of grating/air interface for different metals and grating period of 300 nm (Figure 5.11(b)) is calculated for metal/air interface for a grating period of Λ=300 nm to using Equation (2.1) and compared with the reflection measurements presented in Figure 5.8. The dielectric constants of the metals are taken from Palik [70]. The grey shaded region in the graph indicates the intersection of range of wavelengths where GaN has high absorption and the range of angles in the illumination cone of the lens used in setup. It can be seen that neither gold nor silver metals have available modes within the region of interest, validating the correctness of the metal selection. The PEC curve proves that the geometrical excitation of the evanescent waves plays an important role

in the enhancement. However, when we compare this to the Aluminum we conclude that the spectral behavior of the absorption changes significantly. This proves the role of SPPs in the process.

It can also be seen that, the resonance wavelength shifts toward UV as the incidence angle becomes steeper, which enables higher absorption from GaN active material. The resonance at the 70° incidence angle (that matches the illumination conditions of ellipsometric reflection measurements) in Figure 5.11(b)) are in good agreement with the measured value shown in red curve in Figure 5.8. The resonance behavior depicted in Figure 5.8 is a demonstration of the coupling of SPPs and the resonances are red shifted with the increase in grating period.

Comparison of the overall normalized E-field intensity under the slits with and without the gratings at a resonant and an off-resonant excitation are provided in Figure 5.11(c) and (d) for further visualization of the enhanced transmission at resonant wavelengths. The results show that, there is a significant enhancement where the wavelength is close to the resonance whereas there is not much transmission at an off-resonant wavelength.

The measured spectral photocurrent data for both structures with and without gratings is compared in Figure 5.9(a) along with the calculated enhancement from this measurement shown in Figure 5.9(b). The measurements indicate an 8 fold enhancement at 322 nm for the nano-antenna coupled MSM photodetectors when compared with their counterparts without grating. The measurements are repeated with laser and spectral setups and found to be in agreement. The simulations also predict a similar enhancement behavior as shown in Figure 5.9(b). There is a slight shift between the peaks of experimentally derived and simulated enhancement curves. This mismatch is due to the inadequacy of the simulation software's internal parameter fitting algorithms that could hardly match with the provided GaN data, towards the absorption edge of the material.

The measured current-voltage (IV) characteristics show that, MSM contacts are well isolated although they are spatially close to each other. The measured device break down voltage of 15V proved the superior epitaxial quality of our active GaN material.

5.2.5 Conclusion

To conclude, in this part of the study, a nano-antenna integrated MSM UV photodetector is designed and characterized through measurements and simulations. Spectral and single wavelength reflection measurements were done to determine the plasmonic resonances of various antenna designs with different grating periods. The photodetector characterization was done through responsivity and current I-V measurements. Supporting simulations were done to provide further evidence. Our results indicate an 8 fold enhancement at 322 nm for the nano antenna coupled MSM photodetectors when compared with their counterparts without grating.

Chapter 6

Conclusion

The aim of this thesis was to utilize plasmonics in various applications such as biosensing, Surface Enhanced Raman Spectroscopy and increasing efficiency in MSM UV photodetectors.

In Chapter 3, we studied how LSPR can be employed in biosensing. The main idea was to design a sensor structure that would respond to changes in the refractive index of the surrounding medium which could be detected easily by optical transmission measurements. Silver nano-disk arrays located periodically on a transparent sapphire substrate by Electron-Beam Lithography (EBL) conveniently served for this aim. The resonance behaviour of the nanodisk array was properly tuned for the basic needs of such a detection, namely sharp and intense resonances at the optical frequencies. Transmission/Reflection measurements were taken by a custom set-up at our facilities for optical characterization. Finite difference time domain (FDTD) algorithm based simulations were used both for aiding the design process and for the verification of optical measurements using the physical parameters of the disks determined by SEM. The sensor was first verified by a biotin-avidin bioassay. Real time binding studies showed that the sensor response was saturated within 30 minutes which is much less than the time consumed with classical detection methods such as culture collection or more sophisticated methods such as polymerase chain reaction (PCR) or Enzyme linked immunosorbent assay (ELISA) that is on the order of days. Concentration dependency of the sensor structure was studied. An adequate response at the 1 nM-100 nM range, which can be fitted to a sigmoidal curve as expected was obtained. The refractive index sensitivity of the sensor was determined as 354 nm/RIU for 80 nm nano-disks both with period 150 nm comparable to those obtained in the literature. The idea was

applied detection of heat killed E.Coli bacteria using similar surface functionalization steps and promising results were obtained.

We have investigated efficient substrate designs for Surface Enhanced Raman Spectroscopy in Chapter 4. In the first part of the study, tandem truncated nano-cones composed of Au-SiO_2-Au layers that exhibit highly tunable double resonance behavior were shown to provide increased SERS signal intensity, for the first time. The resonances were tuned to the excitation and Stokes frequencies respectively to provide a better signal enhancement in the SERS experiments. The spatial overlap of the enhanced fields for tandem structures at the two wavelengths was shown to be another important advantage when compared to other designs in literature. EF calculations indicated an enhancement factor of 3.86×10^7. The double resonance design showed a 10 fold better enhancement when compared with their single resonance counterparts. The experimental findings were supported with FDTD simulations, too.

This enhancement is believed to be even more prominent for applications employing well separated laser and Stokes shifted Raman lines such as NIR-SERS which can help overcome the disadvantages of visible lasers such as photochemical reactions, background from fluorescence and degeneration of molecules [100, 119]. Since the excitation and Stokes shifted wavelengths can be more than 200 nm apart from each other in NIR-SERS, a single resonance structure can not provide enhancement at both wavelengths. This can be circumvented with the use of properly tuned double resonance structures as described in this report.

Another application can be Surface Enhanced Hyper Raman Scattering (SEHRS). SEHRS can provide vibrational information on molecules where ordinary Raman Scattering is suppressed and it is much more sensitive to local surface environmental changes than SERS [120]. The scattering signal in SEHRS follow the rule $w=2w_0-\Delta w$, where $2w_0$ is the second harmonic of the excitation frequency and Δw is the vibrational frequency. In this case the two

resonances should be located at w_0 and $2w_0$ as also suggested in previous reports [86].

In the second part of Chapter 4, “coupled” and “etched” concentric ring structures were compared to each other and plain gold film in terms of their SERS signal intensities. The “coupled” concentric ring structures provided Raman signal intensity 630 times larger than plain gold film and 8 times larger than an “etched” concentric ring structure. The increased E-field distribution established between the upper and lower rings due to their coupling was considered to form the basis of the better performance. The increase of “hot spots” responsible for the enhancement was visualized through FDTD simulations, too. The EF is calculated as $1.67x10^7$ for the coupled-concentric ring structures.

Finally, we have studied the utilization of plasmonics for UV-MSM photodetectors in Chapter 5. In the first part, an LSPR enhanced MSM UV photodetector on semi-insulating GaN was presented. Al nanoparticles with plasmonic resonance at UV wavelengths fabricated in between the metallic electrodes of the detector was shown to yield 1.5 fold enhancement in absorption and photocurrent collection at the GaN active layer. Plasmonic enhancement in UV was studied for the first time with this study. In the second part, another UV-MSM photodetector that includes subwavelength apertures surrounded by nano-structured metal gratings was compared to a conventional design without gratings. The gratings were optimized for capturing and delivering more optical power to the absorbing regions of the device. The responsivity values of 1.7 mA/W and 0.2 mA/W were calculated for the samples with and without gratings, respectively. Our results indicated an 8 fold enhancement in the photocurrent at the resonant wavelength of 322 nm. FDTD simulations were done to investigate the physical mechanism behind this enhancement. Surface bound leaky waves and SPPs were considered to be effective mechanisms.

Bibliography

[1] E. Ozbay, "Plasmonics: merging photonics and electronics at nanoscale dimensions," *Science,* vol. 311, no. 5758, pp. 189-193, 2006.

[2] E. Le Ru, P. Etchegoin, J. Grand, N. Félidj, J. Aubard, G. Lévi, A. Hohenau, and J. Krenn, "Surface enhanced Raman spectroscopy on nanolithography-prepared substrates," *Current Applied Physics,* vol. 8, no. 3, pp. 467-470, 2008.

[3] A. J. Haes, C. L. Haynes, A. D. McFarland, G. C. Schatz, R. P. Van Duyne, and S. Zou, "Plasmonic materials for surface-enhanced sensing and spectroscopy," *MRS bulletin,* vol. 30, no. 5, pp. 368-375, 2005.

[4] S. J. Lee, Z. Guan, H. Xu, and M. Moskovits, "Surface-enhanced Raman spectroscopy and nanogeometry: the plasmonic origin of SERS," *The Journal of Physical Chemistry C,* vol. 111, no. 49, pp. 17985-17988, 2007.

[5] J. P. Camden, J. A. Dieringer, J. Zhao, and R. P. Van Duyne, "Controlled plasmonic nanostructures for surface-enhanced spectroscopy and sensing," *Accounts of chemical research,* vol. 41, no. 12, pp. 1653-1661, 2008.

[6] J. N. Anker, W. P. Hall, O. Lyandres, N. C. Shah, J. Zhao, and R. P. Van Duyne, "Biosensing with plasmonic nanosensors," *Nature Materials,* vol. 7, no. 6, pp. 442-453, 2008.

[7] S. Pillai and M. Green, "Plasmonics for photovoltaic applications," *Solar Energy Materials and Solar Cells,* vol. 94, no. 9, pp. 1481-1486, 2010.

[8] V. E. Ferry, M. A. Verschuuren, H. B. T. Li, E. Verhagen, R. J. Walters, R. E. I. Schropp, H. A. Atwater, and A. Polman, "Light trapping in ultrathin plasmonic solar cells," *Optics Express,* vol. 18, no. S2, pp. A237-A245, 2010.

[9] K. Catchpole and A. Polman, "Plasmonic solar cells," *Optics Express,* vol. 16, no. 26, pp. 21793-21800, 2008.

[10] W. Srituravanich, N. Fang, C. Sun, Q. Luo, and X. Zhang, "Plasmonic nanolithography," *Nano Letters,* vol. 4, no. 6, pp. 1085-1088, 2004.

[11] Z. Xie, W. Yu, T. Wang, H. Zhang, Y. Fu, H. Liu, F. Li, Z. Lu, and Q. Sun, "Plasmonic nanolithography: a review," *Plasmonics,* vol. 6, no. 3, pp. 565-580, 2011.

[12] P. G. Kik, S. A. Maier, and H. A. Atwater, "Surface plasmons for nanofabrication," in *Micromachining and Microfabrication,* pp. 215-223, International Society for Optics and Photonics, 2004.

[13] O. Mollet, S. Huant, and A. Drezet, "Scanning plasmonic microscopy by image reconstruction from the Fourier space," *Optics Express,* vol. 20, no. 27, pp. 28923-28928, 2012.

[14] H. A. Atwater, "The promise of plasmonics," *Scientific American,* vol. 296, no. 4, pp. 56-62, 2007.

[15] S. A. Maier, M. L. Brongersma, P. G. Kik, S. Meltzer, A. A. G. Requicha, and H. A. Atwater, "Plasmonics: A Route to Nanoscale Optical Devices," *Advanced Materials,* vol. 13, no. 19, pp. 1501-1505, 2001.

[16] H. J. L. T. W. Ebbesen, H. F. Ghaemi, T. Thio, and P. A. Wolff,, "Extraordinary optical transmission through sub-wavelength hole arrays," *Nature,* vol. 391, no. 6668, pp. 667-669 1998.

[17] E. Hutter and J. H. Fendler, "Exploitation of localized surface plasmon resonance," *Advanced Materials,* vol. 16, no. 19, pp. 1685-1706, 2004.

[18] J. Zhao, X. Zhang, C. R. Yonzon, A. J. Haes, and R. P. Van Duyne, "Localized surface plasmon resonance biosensors," *Nanomedicine,* vol. 1, no. 2, pp. 219-228, 2006.

[19] K. A. Willets and R. P. Van Duyne, "Localized surface plasmon resonance spectroscopy and sensing," *Annual Review of Physical Chemistry,* vol. 58, pp. 267-297, 2007.

[20] ISO 9308-1, "Water quality. Detection and enumeration of Escherichia coli and coliform bacteria. Part 1. Membrane filtration method," 2000

[21] P. Daly, T. Collier, and S. Doyle, "PCR-ELISA detection of Escherichia coli in milk," *Letters in Applied Microbiology,* vol. 34, no. 3, pp. 222-226, 2002.

[22] B. L. Dylla, E. A. Vetter, J. G. Hughes, and F. R. Cockerill, 3rd, "Evaluation of an immunoassay for direct detection of Escherichia coli O157 in stool specimens," *Journal of Clinical Microbiology,* vol. 33, no. 1, pp. 222-225, 1995.

[23] R. P. Johnson, R. J. Durham, S. T. Johnson, L. A. Macdonald, S. R. Jeffrey, and B. T. Butman, "Detection of Escherichia coli O157:H7 in meat by an enzyme-linked immunosorbent assay, EHEC-Tek.," *Applied and Environmental Microbiology,* vol. 61, no. 1, pp. 386-388, 1995.

[24] L. S. Jung, C. T. Campbell, T. M. Chinowsky, M. N. Mar, and S. S. Yee, "Quantitative interpretation of the response of surface plasmon resonance sensors to adsorbed films," *Langmuir,* vol. 14, no. 19, pp. 5636-5648, 1998.

[25] A. J. Haes and R. P. Van Duyne, "A unified view of propagating and localized surface plasmon resonance biosensors," *Analytical and Bioanalytical Chemistry,* vol. 379, no. 7-8, pp. 920-930, 2004.

[26] M. D. Malinsky, K. L. Kelly, G. C. Schatz, and R. P. Van Duyne, "Chain length dependence and sensing capabilities of the localized surface plasmon resonance of silver nanoparticles chemically modified with alkanethiol self-assembled monolayers," *Journal of the American Chemical Society,* vol. 123, no. 7, pp. 1471-1482, 2001.

[27] J. C. Riboh, A. J. Haes, A. D. McFarland, C. R. Yonzon, and R. P. Van Duyne, "A nanoscale optical biosensor: Real-time immunoassay in physiological buffer enabled by improved nanoparticle adhesion," *Journal of Physical Chemistry B,* vol. 107, no. 8, pp. 1772-1780, 2003.

[28] F. Y. Lee, K. H. Fung, T. L. Tang, W. Y. Tam, and C. T. Chan, "Fabrication of gold nano-particle arrays using two-dimensional templates from holographic lithography," *Current Applied Physics,* vol. 9, no. 4, pp. 820-825, 2009.

[29] A. Hohenau, H. Ditlbacher, B. Lamprecht, J. R. Krenn, A. Leitner, and F. R. Aussenegg, "Electron beam lithography, a helpful tool for nanooptics," *Microelectronic Engineering,* vol. 83, no. 4-9, pp. 1464-1467, 2006.

[30] C. Vieu, F. Carcenac, A. Pepin, Y. Chen, M. Mejias, A. Lebib, L. Manin-Ferlazzo, L. Couraud, and H. Launois, "Electron beam lithography: resolution limits and applications," *Applied Surface Science,* vol. 164, no. 1, pp. 111-117, 2000.

[31] A. A. Tseng, K. Chen, C. D. Chen, and K. J. Ma, "Electron beam lithography in nanoscale fabrication: recent development," *Ieee Transactions on Electronics Packaging Manufacturing,* vol. 26, no. 2, pp. 141-149, 2003.

[32] P. Rai-Choudhury, *Handbook of Microlithography, Micromachining, and Microfabrication*. Bellingham, WA, UK: SPIE Optical Engineering Press, 1997.

[33] D. L. Jeanmaire and R. P. Van Duyne, "Surface Raman spectroelectrochemistry: Part I. Heterocyclic, aromatic, and aliphatic amines adsorbed on the anodized silver electrode," *Journal of Electroanalytical Chemistry and Interfacial Electrochemistry,* vol. 84, no. 1, pp. 1-20, 1977.

[34] M. G. Albrecht and J. A. Creighton, "Anomalously intense Raman spectra of pyridine at a silver electrode," *Journal of the American Chemical Society,* vol. 99, no. 15, pp. 5215-5217, 1977.

[35] S. A. Maier, *Plasmonics : fundamentals and applications*. Bath ; New York: Springer, 2006.

[36] K. Kneipp, M. Moskovits, and H. Kneipp, *Surface-Enhanced Raman Scattering: Physics and Applications*. New York: Springer-Verlag, 2006.

[37] A. Campion and P. Kambhampati, "Surface-enhanced Raman scattering," *Chemical Society Reviews,* vol. 27, no. 4, pp. 241-250, 1998.

[38] C. L. Haynes, A. D. McFarland, and R. P. Van Duyne, "Surface-enhanced Raman spectroscopy," *Analytical Chemistry,* vol. 77, no. 17, pp. 338a-346a, 2005.

[39] P. L. Stiles, J. A. Dieringer, N. C. Shah, and R. R. Van Duyne, "Surface-Enhanced Raman Spectroscopy," *Annual Review of Analytical Chemistry,* vol. 1, pp. 601-626, 2008.

[40] M. Moskovits, "Surface-Enhanced Spectroscopy," *Reviews of Modern Physics,* vol. 57, no. 3, pp. 783-826, 1985.

[41] M. Kahl, E. Voges, S. Kostrewa, C. Viets, and W. Hill, "Periodically structured metallic substrates for SERS," *Sensors and Actuators B-Chemical,* vol. 51, no. 1-3, pp. 285-291, 1998.

[42] N. A. Cinel, S. Bütün, and E. Özbay, "Electron beam lithography designed silver nano-disks used as label free nano-biosensors based on localized surface plasmon resonance," *Optics Express,* vol. 20, no. 3, pp. 2587-2597, 2012.

[43] J. Beermann, S. M. Novikov, K. Leosson, and S. I. Bozhevolnyi, "Surface enhanced Raman imaging: periodic arrays and individual metal nanoparticles," *Optics Express,* vol. 17, no. 15, pp. 12698-12705, 2009.

[44] N. Guillot, H. Shen, B. Fremaux, O. Peron, E. Rinnert, T. Toury, and M. L. de la Chapelle, "Surface enhanced Raman scattering optimization of gold nanocylinder arrays: Influence of the localized surface plasmon resonance and excitation wavelength," *Applied Physics Letters,* vol. 97, no. 2, pp. 023113 - 023113-3, 2010.

[45] J. M. Oran, R. J. Hinde, N. Abu Hatab, S. T. Retterer, and M. J. Sepaniak, "Nanofabricated periodic arrays of silver elliptical discs as SERS substrates," *Journal of Raman Spectroscopy,* vol. 39, no. 12, pp. 1811-1820, 2008.

[46] E. Monroy, E. Munoz, F. Sánchez, F. Calle, E. Calleja, B. Beaumont, P. Gibart, J. Munoz, and F. Cussó, "High-performance GaN pn junction photodetectors for solar ultraviolet applications," *Semiconductor science and technology,* vol. 13, no. 9, pp. 1042-1046, 1999.

[47] Q. Chen, M. A. Khan, C. Sun, and J. Yang, "Visible-blind ultraviolet photodetectors based on GaN pn junctions," *Electronics Letters,* vol. 31, no. 20, pp. 1781-1782, 1995.

[48] J. Carrano, T. Li, D. Brown, P. Grudowski, C. Eiting, R. Dupuis, and J. Campbell, "High-speed pin ultraviolet photodetectors fabricated on GaN," *Electronics Letters,* vol. 34, no. 18, pp. 1779-1781, 1998.

[49] Q. Chen, J. Yang, A. Osinsky, S. Gangopadhyay, B. Lim, M. Anwar, M. Asif Khan, D. Kuksenkov, and H. Temkin, "Schottky barrier detectors on GaN for visible–blind ultraviolet detection," *Applied Physics Letters,* vol. 70, no. 17, pp. 2277-2279, 1997.

[50] C. Chen, S. J. Chang, Y. K. Su, G. C. Chi, J. Y. Chi, C. Chang, J. K. Sheu, and J. F. Chen, "GaN metal-semiconductor-metal ultraviolet photodetectors with transparent indium-tin-oxide Schottky contacts," *Photonics Technology Letters, IEEE,* vol. 13, no. 8, pp. 848-850, 2001.

[51] H. Raether, *Surface plasmons : on smooth and rough surfaces and on gratings*. Berlin: Springer-Verlag, 1988.

[52] G. Mie, "Beiträge zur Optik trüber Medien, speziell kolloidaler Metallösungen," *Annalen der Physik,* vol. 330, no. 3, pp. 377-445, 1908.

[53] M. Meier and A. Wokaun, "Enhanced fields on large metal particles: dynamic depolarization," *Optics letters,* vol. 8, no. 11, pp. 581-583, 1983.

[54] H. Kuwata, H. Tamaru, K. Esumi, and K. Miyano, "Resonant light scattering from metal nanoparticles: Practical analysis beyond Rayleigh approximation," *Applied Physics Letters,* vol. 83, no. 22, pp. 4625-4627, 2003.

[55] S. A. Maier and H. A. Atwater, "Plasmonics: Localization and guiding of electromagnetic energy in metal/dielectric structures," *Journal of Applied Physics,* vol. 98, no. 1, pp. 011101-011101-10, 2005.

[56] K. Yee, "Numerical solution of initial boundary value problems involving Maxwell's equations in isotropic media," *Antennas and Propagation, IEEE Transactions on,* vol. 14, no. 3, pp. 302-307, 1966.

[57] E. M. Purcell and C. R. Pennypacker, "Scattering and absorption of light by nonspherical dielectric grains," *The Astrophysical Journal,* vol. 186, pp. 705-714, 1973.

[58] C. V. Raman and K. Krishnan, "A new type of secondary radiation," *Nature,* vol. 121, no. 3048, pp. 501-502, 1928.

[59] M. Fleischmann, P. Hendra, and A. McQuillan, "Raman spectra of pyridine adsorbed at a silver electrode," *Chemical Physics Letters,* vol. 26, no. 2, pp. 163-166, 1974.

[60] R. L. Garrell, "Surface-enhanced Raman spectroscopy," *Analytical Chemistry,* vol. 61, no. 6, pp. 401A-411A, 1989.

[61] M. Kerker, D. S. Wang, and H. Chew, "Surface enhanced Raman scattering (SERS) by molecules adsorbed at spherical particles: errata," *Applied optics,* vol. 19, no. 24, pp. 4159-4174, 1980.

[62] D. S. Wang and M. Kerker, "Enhanced Raman scattering by molecules adsorbed at the surface of colloidal spheroids," *Physical review B,* vol. 24, no. 4, pp. 1777–1790, 1981.

[63] C. L. Haynes and R. P. Van Duyne, "Plasmon-sampled surface-enhanced Raman excitation spectroscopy," *Journal of Physical Chemistry B,* vol. 107, no. 30, pp. 7426-7433, 2003.

[64] A. D. McFarland, M. A. Young, J. A. Dieringer, and R. P. Van Duyne, "Wavelength-scanned surface-enhanced Raman excitation spectroscopy," *Journal of Physical Chemistry B,* vol. 109, no. 22, pp. 11279-11285, 2005.

[65] A. J. Haes and R. P. Van Duyne, "A nanoscale optical biosensor: Sensitivity and selectivity of an approach based on the localized surface plasmon resonance spectroscopy of triangular silver nanoparticles," *Journal of the American Chemical Society,* vol. 124, no. 35, pp. 10596-10604, 2002.

[66] Pierce, "Avidin-Biotin Technical Handbook," ed: Thermo Scientific, 2010.

[67] J. X. Fu, A. Collins, and Y. P. Zhao, "Optical properties and biosensor application of ultrathin silver films prepared by oblique angle deposition," *Journal of Physical Chemistry C,* vol. 112, no. 43, pp. 16784-16791, 2008.

[68] A. J. Haes, W. P. Hall, L. Chang, W. L. Klein, and R. P. Van Duyne, "A localized surface plasmon resonance biosensor: First steps toward an assay for Alzheimer's disease," *Nano Letters,* vol. 4, no. 6, pp. 1029-1034, 2004.

[69] T. Arai, P. K. R. Kumar, C. Rockstuhl, K. Awazu, and J. Tominaga, "An optical biosensor based on localized surface plasmon resonance of silver nanostructured films," *Journal of Optics A: Pure and Applied Optics,* vol. 9, no. 7, pp. 699-703, 2007.

[70] E. D. Palik, *Handbook of Optical Constants of Solids*. New York: Academic Press Inc., 1985.

[71] S. L. Zhu, F. Li, C. L. Du, and Y. Q. Fu, "A localized surface plasmon resonance nanosensor based on rhombic Ag nanoparticle array," *Sensors and Actuators B: Chemical,* vol. 134, no. 1, pp. 193-198, 2008.

[72] B. Sepulveda, P. C. Angelome, L. M. Lechuga, and L. M. Liz-Marzan, "LSPR-based nanobiosensors," *Nano Today,* vol. 4, no. 3, pp. 244-251, 2009.

[73] N. Menon, "Optical biosensors:applying photonics products to the biomedical diagnostics market," presented at the Optical Fiber Communication Conference (OFC), Los Angeles, California, 2004.

[74] G. P. Wiederrecht, *Handbook of Nanoscale Optics and Electronics* Elsevier, 2010.

[75] S. M. Radke and E. C. Alocilja, "A high density microelectrode array biosensor for detection of E. coli O157:H7," *Biosensors and Bioelectronics,* vol. 20, no. 8, pp. 1662-1667, 2005.

[76] C. Ruan, K. Zeng, O. K. Varghese, and C. A. Grimes, "Magnetoelastic immunosensors: amplified mass immunosorbent assay for detection of

Escherichia coli O157:H7," *Analytical Chemistry,* vol. 75, no. 23, pp. 6494-6501, 2003.

[77] A. Subramanian, J. Irudayaraj, and T. Ryan, "A mixed self-assembled monolayer-based surface plasmon immunosensor for detection of E-coli O157 : H7," *Biosensors and Bioelectronics,* vol. 21, no. 7, pp. 998-1006, 2006.

[78] S. L. Zhu, C. L. Du, and Y. Q. Fu, "Localized surface plasmon resonance-based hybrid Au-Ag nanoparticles for detection of Staphylococcus aureus enterotoxin B," *Optical Materials,* vol. 31, no. 11, pp. 1608-1613, 2009.

[79] S. L. Zhu, C. L. Du, and Y. Q. Fu, "Fabrication and characterization of rhombic silver nanoparticles for biosensing," *Optical Materials,* vol. 31, no. 6, pp. 769-774, 2009.

[80] C. D. Chen, S. F. Cheng, L. K. Chau, and C. R. C. Wang, "Sensing capability of the localized surface plasmon resonance of gold nanorods," *Biosensors and Bioelectronics,* vol. 22, no. 6, pp. 926-932, 2007.

[81] M. M. Miller and A. A. Lazarides, "Sensitivity of metal nanoparticle surface plasmon resonance to the dielectric environment," *Journal of Physical Chemistry B,* vol. 109, no. 46, pp. 21556-21565, 2005.

[82] A. Wokaun, "Surface-Enhanced Electromagnetic Processes," *Solid State Physics-Advances in Research and Applications,* vol. 38, pp. 223-294, 1984.

[83] J. Grand, M. L. de la Chapelle, J. L. Bijeon, P. M. Adam, A. Vial, and P. Royer, "Role of localized surface plasmons in surface-enhanced Raman scattering of shape-controlled metallic particles in regular arrays," *Physical review B,* vol. 72, no. 3, pp. 33407-33407-4, 2005.

[84] E. C. Le Ru and P. G. Etchegoin, "Rigorous justification of the [E](4) enhancement factor in Surface Enhanced Raman Spectroscopy," *Chemical Physics Letters,* vol. 423, no. 1-3, pp. 63-66, 2006.

[85] Y. Z. Chu, M. G. Banaee, and K. B. Crozier, "Double-Resonance Plasmon Substrates for Surface-Enhanced Raman Scattering with Enhancement at Excitation and Stokes Frequencies," *Acs Nano,* vol. 4, no. 5, pp. 2804-2810, 2010.

[86] M. G. Banaee, P. Peng, E. D. Diebold, E. Mazur, and K. B. Crozier, "Mixed Dimer Double Resonance Substrates for Surface-Enhanced Raman Spectroscopy," *Acs Nano,* vol. 5, no. 1, pp. 307 - 314, 2010.

[87] Y. Jeyaram, S. K. Jha, M. Agio, J. F. Loffler, and Y. Ekinci, "Magnetic metamaterials in the blue range using aluminum nanostructures," *Optics letters,* vol. 35, no. 10, pp. 1656-1658, 2010.

[88] Y. Ekinci, A. Christ, M. Agio, O. J. F. Martin, H. H. Solak, and J. F. Loffler, "Electric and magnetic resonances in arrays of coupled gold

nanoparticle in-tandem pairs," *Optics Express,* vol. 16, no. 17, pp. 13287-13295, 2008.

[89] A. Baba, A. Kaya, and N. Turk, "Fairy chimneys of Cappadocia and their engineering properties," *Journal of Applied Sciences,* vol. 5, pp. 800-805, 2005.

[90] P. B. Johnson and R. W. Christy, "Optical constants of the noble metals," *Physical review B,* vol. 6, pp. 4370-4379, 1972.

[91] L. J. Wan, M. Terashima, H. Noda, and M. Osawa, "Molecular orientation and ordered structure of benzenethiol adsorbed on gold(111)," *Journal of Physical Chemistry B,* vol. 104, no. 15, pp. 3563-3569, 2000.

[92] C. M. Whelan, M. R. Smyth, and C. J. Barnes, "HREELS, XPS, and electrochemical study of benzenethiol adsorption on Au(111)," *Langmuir,* vol. 15, no. 1, pp. 116-126, 1999.

[93] E. C. Le Ru, E. Blackie, M. Meyer, and P. G. Etchegoin, "Surface enhanced Raman scattering enhancement factors: a comprehensive study," *Journal of Physical Chemistry C,* vol. 111, no. 37, pp. 13794-13803, 2007.

[94] D. A. Genov, A. K. Sarychev, V. M. Shalaev, and A. Wei, "Resonant field enhancements from metal nanoparticle arrays," *Nano Letters,* vol. 4, no. 1, pp. 153-158, 2004.

[95] J. T. Bahns, A. Imre, V. K. Vlasko-Vlasov, J. Pearson, J. M. Hiller, L. H. Chen, and U. Welp, "Enhanced Raman scattering from focused surface plasmons," *Applied Physics Letters,* vol. 91, no. 8, pp. 081104-081104-3, 2007.

[96] G. F. S. Andrade, Min Q; Gordon, R.; Brolo, A. G., "Surface-Enhanced Resonance Raman Scattering on Gold Concentric Rings: Polarization Dependence and Intensity Fluctuations," *The Journal of Physical Chemistry C,* vol. 116, pp. 2672-2676, 2012.

[97] J. M. Steele, Z. W. Liu, Y. Wang, and X. Zhang, "Resonant and non-resonant generation and focusing of surface plasmons with circular gratings," *Optics Express,* vol. 14, no. 12, pp. 5664-5670, 2006.

[98] W. B. Chen, D. C. Abeysinghe, R. L. Nelson, and Q. W. Zhan, "Plasmonic Lens Made of Multiple Concentric Metallic Rings under Radially Polarized Illumination," *Nano Letters,* vol. 9, no. 12, pp. 4320-4325, 2009.

[99] H. Ditlbacher, J. R. Krenn, N. Felidj, B. Lamprecht, G. Schider, M. Salerno, A. Leitner, and F. R. Aussenegg, "Fluorescence imaging of surface plasmon fields," *Applied Physics Letters,* vol. 80, no. 3, pp. 404-406, 2002.

[100] S. Mahajan, M. Abdelsalam, Y. Suguwara, S. Cintra, A. Russell, J. Baumberg, and P. Bartlett, "Tuning plasmons on nano-structured substrates for NIR-SERS," *Physical Chemistry Chemical Physics*, vol. 9, no. 1, pp. 104-9, 2007.

[101] J. J. Miao, Y. S. Wang, C. F. Guo, Y. Tian, S. M. Guo, Q. Liu, and Z. P. Zhou, "Plasmonic Lens with Multiple-Turn Spiral Nano-Structures," *Plasmonics*, vol. 6, no. 2, pp. 235-239, 2011.

[102] H. Ditlbacher, J. R. Krenn, A. Hohenau, A. Leitner, and F. R. Aussenegg, "Efficiency of local light-plasmon coupling," *Applied Physics Letters*, vol. 83, no. 18, pp. 3665-3667, 2003.

[103] L. A. Dick, A. D. McFarland, C. L. Haynes, and R. P. Van Duyne, "Metal film over nanosphere (MFON) electrodes for surface-enhanced Raman spectroscopy (SERS): Improvements in surface nanostructure stability and suppression of irreversible loss," *Journal of Physical Chemistry B*, vol. 106, no. 4, pp. 853-860, 2002.

[104] E. C. Le Ru and P. G. Etchegoin, *Principles of surface-enhanced raman spectroscopy : and related plasmonic effects*. Amsterdam: Elsevier, 2009.

[105] S. Butun, M. Gokkavas, H. B. Yu, and E. Ozbay, "Low dark current metal-semiconductor-metal photodiodes based on semi-insulating GaN," *Applied Physics Letters*, vol. 89, no. 7, pp. 073503-073503-3, 2006.

[106] J. A. Porto, F. J. Garcia-Vidal, and J. B. Pendry, "Transmission resonances on metallic gratings with very narrow slits," *Physical Review Letters*, vol. 83, no. 14, pp. 2845-2848, 1999.

[107] U. Schroter and D. Heitmann, "Surface-plasmon-enhanced transmission through metallic gratings," *Physical review B*, vol. 58, no. 23, pp. 15419-15421, 1998.

[108] M. M. J. Treacy, "Dynamical diffraction in metallic optical gratings," *Applied Physics Letters*, vol. 75, no. 5, pp. 606-608, 1999.

[109] F. J. Garcia-Vidal, H. J. Lezec, T. W. Ebbesen, and L. Martin-Moreno, "Multiple paths to enhance optical transmission through a single subwavelength slit," *Physical Review Letters*, vol. 90, no. 21, pp. 213901-213901-4, 2003.

[110] L. Martin-Moreno, F. J. Garcia-Vidal, H. J. Lezec, A. Degiron, and T. W. Ebbesen, "Theory of highly directional emission from a single subwavelength aperture surrounded by surface corrugations," *Physical Review Letters*, vol. 90, no. 16, pp. 167401-167401-4, 2003.

[111] R. D. R. Bhat, N. C. Panoiu, S. R. J. Brueck, and R. M. Osgood, "Enhancing the signal-to-noise ratio of an infrared photodetector with a circular metal grating," *Optics Express*, vol. 16, no. 7, pp. 4588-4596, 2008.

[112] Z. F. Yu, G. Veronis, S. H. Fan, and M. L. Brongersma, "Design of midinfrared photodetectors enhanced by surface plasmons on grating structures," *Applied Physics Letters,* vol. 89, no. 15, pp. 151116-151116-3, 2006.

[113] T. Ishi, J. Fujikata, K. Makita, T. Baba, and K. Ohashi, "Si nano-photodiode with a surface plasmon antenna," *Japanese Journal of Applied Physics Part 2-Letters & Express Letters,* vol. 44, no. 12-15, pp. L364-L366, 2005.

[114] C. L. Tan, V. V. Lysak, K. Alameh, and Y. T. Lee, "Absorption enhancement of 980 nm MSM photodetector with a plasmonic grating structure," *Optics Communications,* vol. 283, no. 9, pp. 1763-1767, 2010.

[115] N. Das, A. Karar, M. Vasiliev, C. L. Tan, K. Alameh, and Y. T. Lee, "Analysis of nano-grating-assisted light absorption enhancement in metal-semiconductor-metal photodetectors patterned using focused ion-beam lithography," *Optics Communications,* vol. 284, no. 6, pp. 1694-1700, 2011.

[116] A. Karar, N. Das, C. L. Tan, K. Alameh, Y. T. Lee, and F. Karouta, "High-responsivity plasmonics-based GaAs metal-semiconductor-metal photodetectors," *Applied Physics Letters,* vol. 99, no. 13, pp. 133112-133112-3, 2011.

[117] F. J. Garcia-Vidal, L. Martin-Moreno, T. W. Ebbesen, and L. Kuipers, "Light passing through subwavelength apertures," *Reviews of Modern Physics,* vol. 82, no. 1, pp. 729-787, 2010.

[118] D. Brunner, H. Angerer, E. Bustarret, F. Freudenberg, R. Hopler, R. Dimitrov, O. Ambacher, and M. Stutzmann, "Optical constants of epitaxial AlGaN films and their temperature dependence," *Journal of Applied Physics,* vol. 82, no. 10, pp. 5090-5096, 1997.

[119] P. Hendra, C. Jones, and G. Warnes, *Fourier transform Raman spectroscopy : instrumentation and chemical applications*: Prentice Hall, 1991.

[120] J. C. Hulteen, M. A. Young, and R. P. Van Duyne, "Surface-enhanced hyper-Raman scattering (SEHRS) on Ag film over Nanosphere (FON) electrodes: surface symmetry of centrosymmetric adsorbates," *Langmuir,* vol. 22, no. 25, pp. 10354-64, 2006.

Appendix

A. Publication list in SCI journals

1. N. A. Cinel, S. Butun, and E. Özbay, "Electron beam lithography designed silver nanodisks used as label free nano-biosensors based on localized surface plasmon resonance," *Opt Express*, vol. 20, pp. 2587-2597, 2012.
2. N. A. Cinel, S. Bütün, G. Ertaş, and E. Özbay, "Fairy Chimney Shaped Tandem Metamaterials as Double Resonance SERS Substrates," *Small*, published online in October 2012.
3. N. A. Cinel, S. Çakmakyapan, G. Ertaş, and E. Özbay, "Concentric Ring Structures As Efficient Sers Substrates," *JSTQE*, accepted to be published in May/June issue, 2013.
4. S. Bütün, N. A. Cinel, and E. Özbay, "Nanoantenna coupled UV subwavelength photodetectors based on GaN," *Opt Express*, vol. 20, pp. 2649-2656, 2012.
5. S. Bütün, N. A. Cinel, and E. Özbay, "LSPR enhanced MSM UV photodetectors", *Nanotechnology*, vol. 23, pp. 444010-444010-5, 2012.